

Constraining dimension-6 SMEFT with higher-order predictions

for $pp \rightarrow tW$

Nikolaos Kidonakis and Kaan Şimşek

Department of Physics, Kennesaw State University, Kennesaw, Georgia 30144, USA

We study single-top production in association with a W boson at the LHC as a probe of dimension-6 Standard Model Effective Field Theory (SMEFT) at leading order, next-to-leading order, and approximate next-to-next-to-leading order accuracy in QCD. The process is sensitive to operators that modify the top-quark weak and chromomagnetic dipole interactions, and we perform three-parameter linear and quadratic SMEFT fits using doubly differential top-quark distributions in transverse momentum and rapidity for the Run II and Run III configurations at the LHC. We provide a detailed account of the uncertainties and quantify the impact of the different uncertainty components across bins and perturbative orders. We find that effective scales up to 2 TeV can be probed in nonmarginalized fits, while in marginalized fits the corresponding scales are around 0.5 and 1.5 TeV for linear and quadratic fits, respectively.

I. INTRODUCTION

In the LHC era, the Standard Model Effective Field Theory (SMEFT) has become a standard and systematic framework for describing possible heavy new physics through higher-dimensional operators. A complete nonredundant dimension-6 basis, the Warsaw basis, was established in 2010 [1], and equivalent alternative organizations such as the Higgs basis and the Strongly Interacting Light Higgs basis were developed and related back to it by field redefinitions [2, 3]. The operator program has since been pushed to higher orders, including complete dimension-8 bases and progress toward even higher dimensions [4–6], supported by systematic enumeration tools such as Hilbert-series methods [7–10]. In parallel, the SMEFT toolkit has matured through the derivation of complete Feynman rules and public implementations enabling automated predictions [11–15], together with extensive studies of renormalization, operator mixing, and fundamental consistency conditions, including pos-

itivity bounds that restrict parts of parameter space under assumptions like a causal and unitary ultraviolet (UV) completion [16–18]. Recently, the complete set of one-loop threshold corrections in the dimension-6 SMEFT, relating broken-phase electroweak inputs to $\overline{\text{MS}}$ symmetric-phase parameters and providing a process-independent ingredient for RG running and matching, was computed in analytical form [19]. A broad overview can be found in [20].

Phenomenologically, the SMEFT has been used to interpret data and constrain new physics from early sector-by-sector studies, such as electroweak precision tests, four-fermion interactions, Higgs and gauge-boson observables, and complementary low-energy and flavor measurements, to increasingly comprehensive global analyses [21–28]. As LHC measurements improved, the program shifted toward global fits combining Higgs, electroweak, and top-quark observables with correlations and growing scope across many Wilson coefficients [29–37], sometimes supplemented by heavy-flavor and low-energy inputs or controlled by flavor assumptions, and in some cases incorporating uncertainties deriving from parton distribution functions (PDFs) directly into the effective field theory (EFT) treatment [38, 39]. More recently, there has also been rising attention to effects beyond leading dimension-6 order, including explicit dimension-8 contributions and more general higher-order terms in SMEFT parameters, with studies exploring their impact on diboson, Drell-Yan, and Higgs observables [40–44]. The SMEFT approach is now also routinely used by the experimental community, for example in recent CMS EFT interpretations [45].

For phenomenological applications, the limiting factor is often theoretical accuracy; namely, turning precision measurements into meaningful constraints on Wilson coefficients requires predictions that are computed consistently in the EFT expansion and at sufficiently high perturbative order. This has motivated substantial progress on SMEFT calculations beyond leading order (LO), with a range of next-to-leading order (NLO) studies now available [46–52]. On the practical side, automated NLO QCD computations in the SMEFT can be performed in `MADGRAPH5_AMC@NLO` [53] through the `SMEFT@NLO` package [54].

Top-quark production processes provide opportunities for the study of the SMEFT and its effective higher-dimensional operators. In Ref. [55], calculations at approximate next-to-next-to-leading order (aNNLO) were performed for the chromomagnetic dipole operator in top-antitop pair production. In this study, we use higher-order calculations for the associated production of a top quark with a W boson (tW production) to constrain dimension-6 SMEFT

operators.

The tW process has the second largest cross section among single-top production processes at LHC energies, and many cross-section measurements have been taken by ATLAS and CMS [56–68]. Results for tW production and decays appeared at LO in Refs. [69–72], and with some additional corrections in [73, 74]. The full NLO cross section for this process was presented in Refs. [75–77]. NLO calculations with decays of the top quark and the W boson were made in Ref. [76], and with parton showers in [78, 79]. Some progress towards 2-loop QCD amplitudes was made in [80–85].

The calculation of soft-gluon corrections beyond NLO from QCD threshold resummation was studied for tW production in a series of papers in Refs. [86–95], where cross sections and differential distributions at aNNLO and higher were presented (see also [86, 87, 89–91, 93, 94, 96–99] for other single-top processes). The soft-gluon corrections are large and numerically dominant, and thus it is important to calculate these contributions beyond NLO. Higher-order results based on resummation in another formalism, namely Soft-Collinear Effective Theory, have appeared in [100–102].

This paper is organized as follows. In Sec. II, we describe tW^- production at the LHC within the SMEFT framework and define the set of dimension-6 operators and Wilson coefficients relevant to our analysis. In Sec. III, we briefly describe the formalism for the calculation of the soft-gluon corrections used to construct the aNNLO predictions. In Sec. IV, we describe the numerical setup, present the Standard Model (SM) and SMEFT distributions, and detail our statistical treatment and uncertainty modeling. In Sec. V, we present the SMEFT fit results. We conclude in Sec. VI.

II. tW PRODUCTION AT THE LHC WITHIN THE SMEFT

The SMEFT is a model-independent extension of the SM in which one builds operators $O_k^{(n)}$ of mass dimension $n > 4$ at a UV scale Λ beyond accessible collider energy using the existing SM spectrum and introduces Wilson coefficients $C_k^{(n)}$ as effective couplings. The SMEFT Lagrangian is schematically given by

$$\mathcal{L} = \mathcal{L}_{\text{SM}} + \sum_{n>4} \frac{1}{\Lambda^{n-4}} \sum_k C_k^{(n)} O_k^{(n)}. \quad (1)$$

The SMEFT Lagrangian shifts the SM vertices in a gauge-invariant manner and respects all underlying symmetries. Here, we focus on the case $n = 6$.

In this work, we adopt the $\{G_F, m_Z, m_W\}$ scheme, as it is the natural choice for LHC processes with external W bosons. The choice necessarily affects the operators involved. In order to be consistent in our calculations at various orders, we borrow the Feynman rules from the SMEFT@NLO model file [54]. We adopt the five-flavor scheme and set the Cabibbo-Kobayashi-Maskawa (CKM) matrix element $V_{tb} = 1$, while V_{ts} and V_{td} are taken to vanish. This choice is standard in single-top analyses, as off-diagonal contributions are suppressed by both the CKM hierarchy and the small parton luminosities for d and s quarks.

We consider the hadronic process $pp \rightarrow tW^-$. The underlying partonic process at leading order is $gb \rightarrow tW^-$. The Feynman diagrams at leading order are presented in Fig. 1. The double lines with an arrow indicate the top quark.

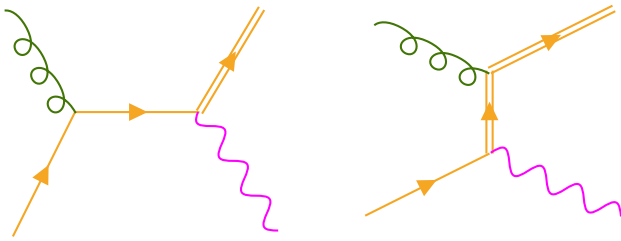


FIG. 1. The Feynman diagrams for the partonic process contributing to $pp \rightarrow tW^-$ at leading order.

There are two classes of dimension-6 SMEFT operators of interest from the Warsaw basis [1] presented in Table I. First, we have the operators that directly modify the qgg and tBW vertices at leading order in SMEFT parameters. These are weak and chromomagnetic couplings, as well as the couplings of the quark current to operators of the form $[\varphi D\varphi]$. The second class of operators is the ones that enter through the input parameters.

TABLE I. The dimension-6 SMEFT operators from the Warsaw basis [1] that affect the observable at leading order in Wilson coefficients.

Couplings	Input parameters
$O_{dG} = [\bar{q}\sigma^{\mu\nu}T^A d]\varphi G_{\mu\nu}^A$	$O_{\ell\ell} = [\bar{\ell}\gamma_\mu\ell][\bar{\ell}\gamma^\mu\ell]$
$O_{uG} = [\bar{q}\sigma^{\mu\nu}T^A u]\tilde{\varphi} G_{\mu\nu}^A$	$O_{\varphi\ell}^{(3)} = [\varphi^\dagger i \overset{\leftrightarrow}{D}_\mu \varphi][\bar{\ell}\tau^I \gamma^\mu \ell]$
$O_{dW} = [\bar{q}\sigma^{\mu\nu}d]\tau^I \varphi W_{\mu\nu}^I$	
$O_{uW} = [\bar{q}\sigma^{\mu\nu}u]\tau^I \tilde{\varphi} W_{\mu\nu}^I$	
$O_{\varphi q}^{(3)} = [\varphi^\dagger i \overset{\leftrightarrow}{D}_\mu \varphi][\bar{q}\tau^I \gamma^\mu q]$	
$O_{\varphi ud} = i[\tilde{\varphi}^\dagger \overset{\leftrightarrow}{D}_\mu \varphi][\bar{u}\gamma^\mu d]$	

In Table I, ℓ and q denote the left-handed $SU(2)_L$ lepton and quark doublets, while u and d are the corresponding right-handed $SU(2)_L$ singlets, with generation indices suppressed; $\bar{\psi} \equiv \psi^\dagger \gamma^0$. φ is the $SU(2)_L$ scalar doublet, with $\tilde{\varphi} \equiv i\tau^2 \varphi^*$ its charge-conjugate. D_μ is the SM covariant derivative, and the τ^I are the Pauli matrices acting on $SU(2)_L$ indices, with the left-right derivative defined such that

$$\varphi^\dagger i \overset{\leftrightarrow}{D}_\mu \varphi = i\varphi^\dagger (D_\mu - \overset{\leftarrow}{D}_\mu) \varphi, \quad (2)$$

$$\varphi^\dagger i \overset{\leftrightarrow}{D}_\mu^I \varphi = i\varphi^\dagger (\tau^I D_\mu - \overset{\leftarrow}{D}_\mu \tau^I) \varphi, \quad (3)$$

with $\varphi^\dagger \overset{\leftarrow}{D}_\mu \varphi = (D_\mu \varphi^\dagger) \varphi$, while the T^A are the $SU(3)_c$ generators acting on color indices. $W_{\mu\nu}^I$ and $G_{\mu\nu}^A$ are the gauge field strength tensors for $SU(2)_L$ and for $SU(3)_c$, respectively. The Dirac matrices γ^μ and $\sigma^{\mu\nu} \equiv \frac{i}{2}[\gamma^\mu, \gamma^\nu]$ appear in the fermion bilinears; square brackets indicate Lorentz and gauge-invariant contractions within each bilinear/current, with implicit contraction of spinor, $SU(2)_L$, and color indices as appropriate.

With a massless bottom quark, the operators O_{dG} , O_{dW} , and $O_{\varphi ud}$ do not contribute because they involve chirality flip. With that, we are left with only five operators, now explicitly written in the *top basis* [54]: O_{tG} , O_{tW} , $O_{\varphi Q}^{(3)}$, $O_{\ell\ell}$, and $O_{\varphi\ell}^{(3)}$. With real Wilson coefficients (since we are not immediately interested in CP -violating effects), the relevant Feynman rules from [54] can be summarized as follows:

$$V_{ttg}^\mu = 2i\sqrt{\pi\alpha_s} T_{ab}^A \left\{ \gamma^\mu - \frac{2^{1/4} C_{tG}}{\sqrt{G_F} \Lambda^2} i\sigma^{\mu\nu} p_{3\nu} \right\}, \quad (4)$$

$$V_{bbg}^\mu = 2i\sqrt{\pi\alpha_s} T_{ab}^A \gamma^\mu, \quad (5)$$

$$V_{tbW}^\mu = 2^{3/4} i \sqrt{G_F} m_W \left\{ \gamma^\mu P_L - \frac{C_{tW}}{G_F m_W \Lambda^2} i \sigma^{\mu\nu} p_{3\nu} P_L + \frac{C_p}{2\sqrt{2} G_F \Lambda^2} \gamma^\mu P_L \right\}, \quad (6)$$

where we have defined $C_p = 2C_{\varphi Q}^{(3)} + C_{\ell\ell}^{[1221]} - C_{\varphi\ell}^{(3)[11]} - C_{\varphi\ell}^{(3)[22]}$, with the numbers in square brackets indicating the generation indices; the Feynman rules are illustrated in Fig. 2. Since three of the operators of interest appear only in a certain linear combination, at the end of the day we have only three Wilson coefficients of interest: C_{tG} , C_{tW} , and C_p .

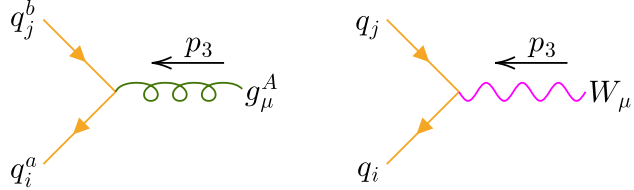


FIG. 2. The relevant SMEFT Feynman rules for the partonic process of interest, adopted from [54].

The hadronic cross section at the pp center-of-mass (c.m.) energy s is computed as

$$\sigma(s) = \sum_{i=-N_f}^{N_f} \sum_{j=-N_f}^{N_f} \int dx_1 dx_2 f_i(x_1, \mu_F) f_j(x_2, \mu_F) \sigma_{ij}(\hat{s}), \quad (7)$$

where N_f is the number of active flavors, i and j are the flavor indices with the negative values indicating antiquarks and 0 the gluon, x_1 and x_2 are the Bjorken- x parameters for the incoming partons, f_i and f_j are the parton distribution functions (PDFs) defined at the factorization scale μ_F , and σ_{ij} is the partonic cross section corresponding to the partonic process $f_i f_j \rightarrow tW^-$ given by

$$\sigma_{ij}(\hat{s}) = F \int \overline{|\mathcal{A}_{ij}|^2} d\text{LIPS}, \quad (8)$$

where \hat{s} is the c.m. energy for the partonic process, $F = 1/(2\hat{s})$ is the flux factor for massless initial states and $d\text{LIPS}$ is the two-particle Lorentz-invariant phase space. Here, $\overline{|\mathcal{A}_{ij}|^2}$ denotes the spin and color-averaged squared amplitude for the said partonic process and the only contributions at leading order are the bg and gb processes.

We parametrize the cross section as

$$\sigma = \sigma_{\text{SM}} + \sum_k C_k \sigma_k + \sum_{k \leq k'} C_k C_{k'} \sigma_{kk'}. \quad (9)$$

at all orders. For the leading-order amplitudes, we use FEYNARTS [103] and FEYNCALC [104–107]. For the partonic process

$$b(p_1) + g(p_2) \rightarrow t(p_3) + W^-(p_4), \quad (10)$$

the squared SM amplitude is obtained to be

$$\begin{aligned} \overline{|\mathcal{A}_{bg}|^2}_{\text{SM}} = & \frac{2\sqrt{2}\pi G_F \alpha_s}{3\hat{s}(m_t^2 - \hat{u})^2} \left\{ m_t^4 \left(-2\hat{u}m_W^2 - 2m_W^4 + (\hat{s} + \hat{u})^2 \right) \right. \\ & + m_t^2 \left(2m_W^2 (-\hat{s}\hat{u} + \hat{s}^2 + 2\hat{u}^2) - 2\hat{u}m_W^4 + 4m_W^6 - \hat{u}(\hat{s} + \hat{u})^2 \right) \\ & \left. - m_t^6 (2\hat{s} + \hat{u}) - 2\hat{u}m_W^2 (-2m_W^2(\hat{s} + \hat{u}) + 2m_W^4 + \hat{s}^2 + \hat{u}^2) + m_t^8 \right\}. \quad (11) \end{aligned}$$

Here, we have defined $\hat{s} = (p_1 + p_2)^2$, $\hat{t} = (p_1 - p_3)^2$, and $\hat{u} = (p_1 - p_4)^2$, which satisfy $\hat{s} + \hat{t} + \hat{u} = m_t^2 + m_W^2$ at leading order. The shifts to the squared amplitude for the bg process characterized by C_k and $C_k C_{k'}$ are presented in Tables II and III. The gb channel is given by $\hat{u} \rightarrow \hat{t}$.

TABLE II. Linear corrections to the squared SMEFT amplitude. The expressions in the second column are to be multiplied by $\frac{2\pi\alpha_s}{3\Lambda^2\hat{s}(m_t^2 - \hat{u})^2}$.

C_k	$\overline{ \mathcal{A}_{bg} ^2}_k$
C_{tG}	$2 \cdot 2^{3/4} \hat{s} \sqrt{G_F} m_t m_W^2 (m_t^2 - \hat{u}) \left\{ m_t^2 + 2\hat{s} - \hat{u} \right\}$
C_{tW}	$2\sqrt{2} m_t m_W \left\{ -m_t^4 (6m_W^2 + 2\hat{s} + 3\hat{u}) + m_t^2 (6m_W^4 - (\hat{s} - \hat{u})(\hat{s} + 3\hat{u})) \right. \\ \left. + \hat{u} (6m_W^2(\hat{s} + \hat{u}) - 6m_W^4 + (\hat{s} - 3\hat{u})(\hat{s} + \hat{u})) + 3m_t^6 \right\}$
C_p	$m_t^4 \left(-2\hat{u}m_W^2 - 2m_W^4 + (\hat{s} + \hat{u})^2 \right) \\ + m_t^2 \left(2m_W^2 (-\hat{s}\hat{u} + \hat{s}^2 + 2\hat{u}^2) - 2\hat{u}m_W^4 + 4m_W^6 - \hat{u}(\hat{s} + \hat{u})^2 \right) \\ - m_t^6 (2\hat{s} + \hat{u}) - 2\hat{u}m_W^2 (-2m_W^2(\hat{s} + \hat{u}) + 2m_W^4 + \hat{s}^2 + \hat{u}^2) + m_t^8$

TABLE III. Quadratic corrections to the squared SMEFT amplitude. The expressions in the second column are to be multiplied by $\frac{\pi\alpha_s}{6\sqrt{2}\Lambda^4\hat{s}G_F(m_t^2-\hat{u})^2}$.

$C_k C_{k'}$	$ \mathcal{A}_{bg} ^2_{kk'}$
C_{tG}^2	$-8\sqrt{2}\hat{s}G_F(m_t^2-\hat{u})^2\left\{-2m_W^2(\hat{s}+\hat{u})+m_t^2(m_W^2-\hat{u})+2m_W^4+\hat{s}\hat{u}\right\}$
$C_{tG}C_{tW}$	$-16\sqrt[4]{2}\hat{s}\sqrt{G_F}m_W(m_t^2-\hat{u})^2\left\{m_W^2-2\hat{u}\right\}$
$C_{tG}C_p$	$4\cdot2^{3/4}\hat{s}\sqrt{G_F}m_tm_W^2(m_t^2-\hat{u})\left\{m_t^2+2\hat{s}-\hat{u}\right\}$
C_{tW}^2	$8\left\{-m_t^6(3m_W^2+4\hat{s}+2\hat{u})+m_t^4(-m_W^2(2\hat{s}+\hat{u})+2m_W^4+2(4\hat{s}\hat{u}+\hat{s}^2+\hat{u}^2))\right.$ $+m_t^2(m_W^2(\hat{s}+\hat{u})(\hat{s}+5\hat{u})-4\hat{u}m_W^4+2m_W^6-2\hat{u}(6\hat{s}\hat{u}+3\hat{s}^2+\hat{u}^2))$ $\left.-\hat{u}\left(-2m_W^4(\hat{s}+\hat{u})+m_W^2(\hat{s}+\hat{u})^2+2m_W^6-4\hat{s}\hat{u}(\hat{s}+\hat{u})\right)+2m_t^8\right\}$
$C_{tW}C_p$	$4\sqrt{2}m_tm_W\left\{-m_t^4(6m_W^2+2\hat{s}+3\hat{u})+m_t^2(6m_W^4-(\hat{s}-\hat{u})(\hat{s}+3\hat{u}))\right.$ $\left.+\hat{u}(6m_W^2(\hat{s}+\hat{u})-6m_W^4+(\hat{s}-3\hat{u})(\hat{s}+\hat{u}))\right)+3m_t^6\right\}$
C_p^2	$m_t^4\left(-2\hat{u}m_W^2-2m_W^4+(\hat{s}+\hat{u})^2\right)$ $+m_t^2\left(2m_W^2(-\hat{s}\hat{u}+\hat{s}^2+2\hat{u}^2)-2\hat{u}m_W^4+4m_W^6-\hat{u}(\hat{s}+\hat{u})^2\right)$ $-m_t^6(2\hat{s}+\hat{u})-2\hat{u}m_W^2(-2m_W^2(\hat{s}+\hat{u})+2m_W^4+\hat{s}^2+\hat{u}^2)+m_t^8$

At NLO QCD, the real-emission contributions to $pp \rightarrow tW^-$ contain diagrams with an intermediate resonant \bar{t} , corresponding to $pp \rightarrow t\bar{t}$ followed by $\bar{t} \rightarrow W^-\bar{b}$, and thus overlap with the tW^- signal definition. To avoid double counting with the $t\bar{t}$ channel, we adopt the diagram-removal prescription and exclude the resonant \bar{t} contributions in our NLO predictions, following the implementation within SMEFT@NLO [54] in MADGRAPH5_AMC@NLO [53].

III. SOFT-GLUON CORRECTIONS

In this section, we review the soft-gluon resummation formalism that we use for the calculation of soft-gluon corrections through NNLO for tW production [86–95]. In addition to the kinematical variables \hat{s} , \hat{t} , and \hat{u} that we defined previously for the $bg \rightarrow tW^-$ partonic process, we also introduce the variable $s_4 = \hat{s} + \hat{t} + \hat{u} - m_t^2 - m_W^2$ which vanishes at partonic threshold where there is no energy available for additional radiation.

The soft-gluon corrections appear in the perturbative series for the cross section via plus distributions involving s_4 , specifically $[(\ln^k(s_4/m_t^2))/s_4]_+$, where k takes values from 0 to

$2n - 1$ in the n th order corrections in the strong coupling.

The resummation of soft-gluon contributions follows as a consequence of the factorization of the cross section into functions that describe soft and collinear emission in the partonic process. We take Laplace transforms of the partonic scattering cross section, $\hat{\sigma}(N) = \int(ds_4/s) e^{-Ns_4/s} \hat{\sigma}(s_4)$, with N the transform variable, and write a factorized expression:

$$\sigma_{bg \rightarrow tW}(N) = H_{bg \rightarrow tW} S_{bg \rightarrow tW} \left(\frac{m_t}{N\mu} \right) \psi_b(N_b) \psi_g(N_g), \quad (12)$$

where μ is the scale, $H_{bg \rightarrow tW}$ is the hard-scattering function, $S_{bg \rightarrow tW}$ is the soft-gluon function for non-collinear soft-gluon emission, and ψ_b and ψ_g are functions which describe soft and collinear emission from, respectively, the incoming bottom quark and gluon. The soft function $S_{bg \rightarrow tW}$ requires renormalization and its N -dependence can be resummed via renormalization group evolution.

The resummed partonic cross section takes the form

$$\begin{aligned} \sigma_{bg \rightarrow tW}^{res}(N) = & \exp \left[\sum_{i=b,g} E_i(N_i) \right] H_{bg \rightarrow tW}(\alpha_s(\sqrt{s})) S_{bg \rightarrow tW}(\alpha_s(\sqrt{s}/\tilde{N})) \\ & \times \exp \left[2 \int_{\sqrt{s}}^{\sqrt{s}/\tilde{N}} \frac{d\mu}{\mu} \Gamma_{S_{bg \rightarrow tW}}(\alpha_s(\mu)) \right] \end{aligned} \quad (13)$$

where the exponents E_i resum universal collinear and soft emissions from the incoming partons, and $\Gamma_{S_{bg \rightarrow tW}}$ is the soft anomalous dimension which resums noncollinear soft-gluon contributions in this process. More details and explicit expressions for these quantities can be found in Refs. [86–95].

By expanding the resummed cross section to fixed order and, then, inverting back to momentum space, we derive results for soft-gluon corrections through NNLO without any need for a prescription. Thus, we calculate aNNLO cross sections that are matched to NLO as described in the next section.

IV. NUMERICAL ANALYSIS

In this section, we detail our calculations for the numerical analysis. We carry out the calculations at leading order (LO), approximate next-to-leading order (aNLO), and unmatched approximate next-to-next-to-leading order (uaNNLO) using in-house codes. We

use LHAPDF [108] and VEGAS [109, 110] for Python, and at next-to-leading order (NLO) we use MADGRAPH5_AMC@NLO [53] in conjunction with NINJA [111–113] and COLLIER [114]. The matched approximate next-to-next-to-leading (aNNLO) order is then obtained by using the relation

$$a\text{NNLO} = \text{NLO} - a\text{NLO} + u a\text{NNLO}, \quad (14)$$

where aNLO is given by the LO calculations plus the first-order soft-gluon corrections.

The numerical values of the parameters are given by

$$G_F = 1.1663788 \times 10^{-5} \text{ GeV}^{-2}, \quad (15)$$

$$m_t = 172.5 \text{ GeV}, \quad (16)$$

$$m_Z = 91.1880 \text{ GeV}, \quad (17)$$

$$m_W = 80.3692 \text{ GeV}. \quad (18)$$

The renormalization and factorization scales are fixed at $\mu_R = \mu_F = \mu_0 = m_t$ and we consider variations $\mu_R = f_R \mu_0$ and $\mu_F = f_F \mu_0$ with $f_R, f_F \in \{0.5, 1, 2\}$. We use the MSHT20 NLO and NNLO PDFs [115]. We assume $N_f = 5$, and the running of the strong coupling α_s is provided from the PDF set. We set $\Lambda = 1 \text{ TeV}$. We impose basic fiducial acceptance requirements on the reconstructed top quark,

$$|y| < 3, \quad p_T > 30 \text{ GeV}, \quad (19)$$

where the transverse momentum threshold serves to exclude the near-threshold region and ensures infrared-safe and numerically stable predictions in the binned analysis. We consider the binning

$$p_T \in [30, 50, 80, 120, 160, 200, 250] \text{ GeV}, \quad (20)$$

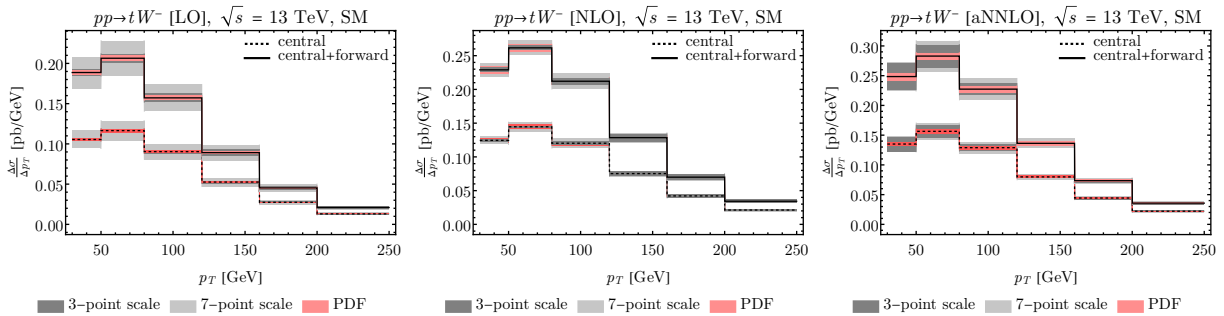
$$0 < |y| < 1, \quad 1 < |y| < 3. \quad (21)$$

We refer to the first y region as *central* and the second as *forward*. Thus, in total, we have 12 bins presented in Table IV. We assume an integrated luminosity of $\mathcal{L} = 139 \text{ fb}^{-1}$ for 13 TeV (Run II) and $\mathcal{L} = 300 \text{ fb}^{-1}$ for 13.6 TeV (Run III). Experimental systematics are modeled by a 5% per-bin uncorrelated efficiency/selection uncertainty and a 1.7% fully correlated luminosity uncertainty. We introduce fully correlated PDF uncertainties and uncorrelated scale variations as theoretical uncertainties.

TABLE IV. The top-quark transverse momentum and rapidity bins assumed in our analysis.

Bin	p_T [GeV]	y	Bin	p_T [GeV]	y
1	[30, 50]	<i>central</i>	7	[120, 160]	<i>central</i>
2	[30, 50]	<i>forward</i>	8	[120, 160]	<i>forward</i>
3	[50, 80]	<i>central</i>	9	[160, 200]	<i>central</i>
4	[50, 80]	<i>forward</i>	10	[160, 200]	<i>forward</i>
5	[80, 120]	<i>central</i>	11	[200, 250]	<i>central</i>
6	[80, 120]	<i>forward</i>	12	[200, 250]	<i>forward</i>

The top-quark distributions across the bins in tW^- production in the SM together with 3-point and 7-point scale variations, as well as PDF uncertainties, at LO, NLO, and aNNLO at 13 TeV are given in Fig. 3. In this figure, the dashed line indicates the *central* rapidity contribution at a given p_T bin, whereas the solid line is the *central* and *forward* contributions combined. The dark gray shade indicates the 3-point scale variation, light gray the 7-point scale variation, and red the PDF variations. In the aNNLO distribution, we propagate PDF uncertainties by applying the same relative PDF variation observed at NLO. We have verified that this prescription reproduces the aNNLO PDF dependence to excellent accuracy for the distributions considered. The pictured behavior is similar for the 13.6 TeV distributions.

FIG. 3. The top-quark distributions in tW^- production in the SM across the assumed bins at LO (left), NLO (center), and aNNLO (right) at 13 TeV.

For the Run II (III) configuration, at LO, the PDF uncertainties range from 1.6% (1.6%) to 2.5% (2.4%) and the 3-point scale variations from 1.5% (1.3%) to 6.0% (5.7%), and the 7-point scale variations are about 11% (11%) and do not vary considerably. At NLO, the PDF uncertainties are about 2.5% (2.5%), and the 3-point scale uncertainties vary between

0.94% (0.24%) and 7.3% (7.8%), whereas the 7-point scale variations range from 4.0% (4.4%) to 8.1% (8.3%). At aNNLO, the PDF percentage uncertainties are the same as NLO, and the 3-point scale variations range from 1.5% (1.6%) to 9.2% (8.2%) and the 7-point scale uncertainties from 5.9% (5.1%) to 9.7% (10%). We choose 3-point variations as the basis for scale variations in the rest of the work.

In Fig. 4, we compare the LO, NLO, and aNNLO distributions and also present the k -factors across the assumed bins at 13 TeV within the SM. On the left panel, the black line indicates the LO, red NLO, and blue aNNLO; on the right, the black line is the k -factor for NLO and LO, red for aNNLO and LO, and blue for aNNLO and NLO. On both panels, the dashed line represents the *central* rapidity contributions at a given p_T bin and the solid one the combined *central* and *forward* contributions. The k factor is nearly flat for aNNLO/NLO, varying only mildly around ~ 1.08 across the assumed bins. In contrast, the NLO/LO and aNNLO/LO k factors exhibit a clear increase with p_T .

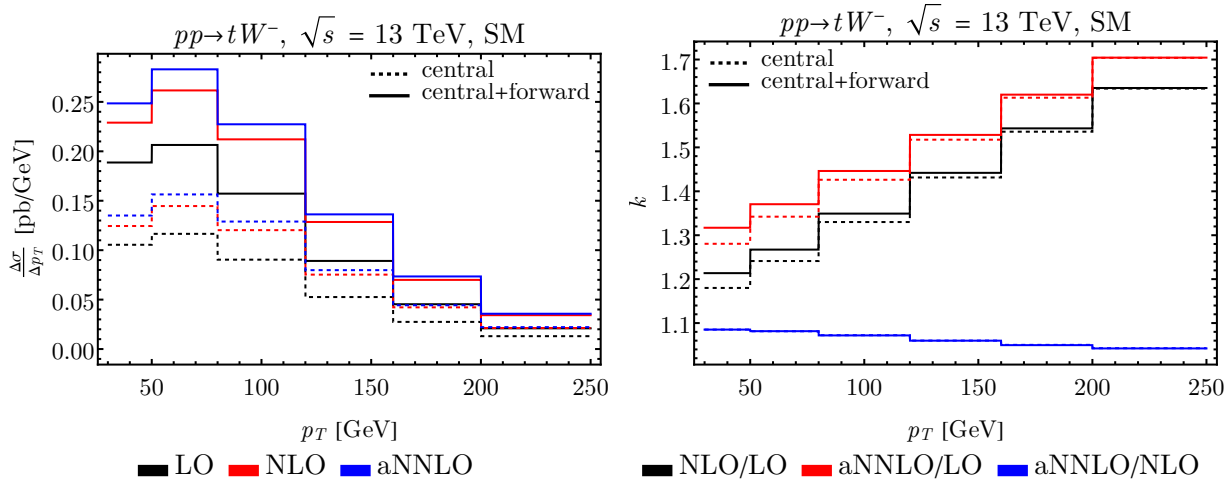


FIG. 4. Comparison of LO, NLO, and aNNLO SM distributions (left) at 13 TeV, together with the corresponding k factors (right) across the assumed bins.

In Fig. 5 and 6, we present the linear and diagonal quadratic SMEFT contributions, respectively, to the top distributions relative to the SM in units of percent at LO, NLO, and aNNLO at 13 TeV. Here, the red line is for C_{tG} , blue for C_{tW} , and green for C_p . The dashed curve is for the *central* rapidity contributions and solid for the combined *central* and *forward* contributions. We observe that the linear SMEFT correction characterized by C_p is at around 6% and is essentially flat across bins at LO. Once higher-order effects are included,

it develops small but noticeable bin-to-bin variations. The linear corrections associated with C_{tG} and C_{tW} are at around 8% and exhibit mild shape dependence. A similar pattern holds for the diagonal quadratic terms. The C_p^2 contribution is around 0.1% at LO with little to no bin sensitivity, but including running Wilson coefficients at higher orders again induces small yet visible variations. In contrast, the C_{tG}^2 and C_{tW}^2 contributions show a pronounced p_T dependence, growing significantly toward the higher end. As anticipated, the sensitivity gets stronger toward larger p_T ; however, this is the far tail where the tW signal yield is already small. The behavior is similar for 13.6 TeV.

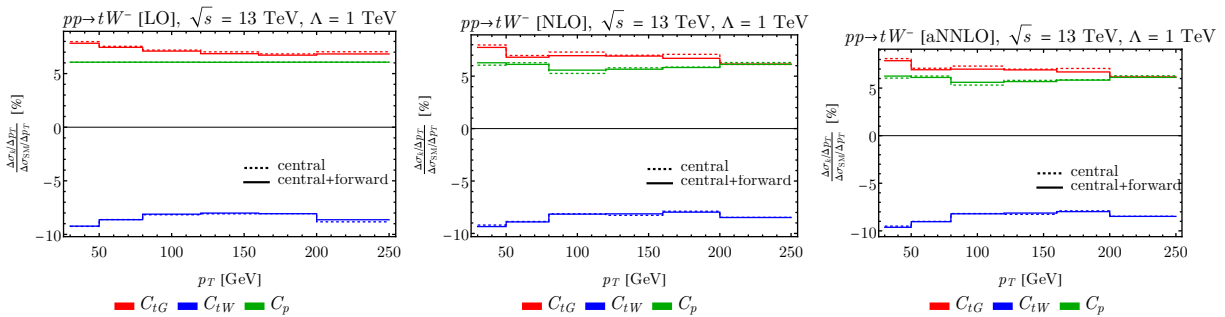


FIG. 5. Linear SMEFT corrections to the top distributions characterized by C_{tG} , C_{tW} , and C_p relative to the SM in percent at LO (left), NLO (center), and aNNLO (right) at 13 TeV.

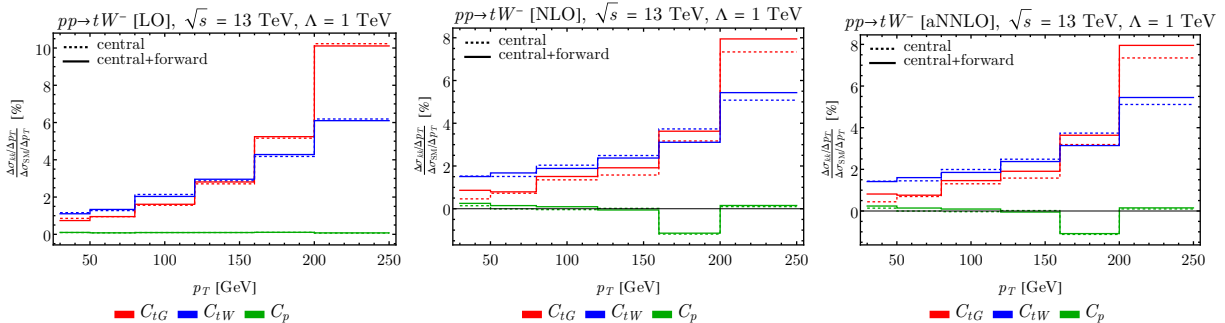


FIG. 6. The same as Fig. 5 but for diagonal quadratic corrections characterized by C_{tG}^2 , C_{tW}^2 , and C_p^2 .

We now describe our statistical procedure. We perform linear and quadratic SMEFT fits at dimension 6 on the three Wilson coefficients of interest C_{tG} , C_{tW} , and C_p . We choose the doubly differential cross section as our observable. For our fitting, we perform a standard

χ^2 test statistics. We define

$$\chi^2 = (\mathcal{O} - \hat{\mathcal{O}})^\top \mathcal{H}(\mathcal{O} - \hat{\mathcal{O}}), \quad (22)$$

where \mathcal{O} is the pseudodata, $\hat{\mathcal{O}}$ is the model function, namely the observable linear or quadratic in SMEFT parameters, and $\mathcal{H} = \mathcal{E}^{-1}$ is the inverse of the uncertainty matrix, \mathcal{E} . We start with the uncertainty matrix. It has two parts, experimental and theoretical:

$$\mathcal{E} = \mathcal{E}^{\text{exp}} + \mathcal{E}^{\text{theo}}. \quad (23)$$

Here, the experimental part is given by

$$\mathcal{E}_{bb'}^{\text{exp}} = I_{bb'} (\delta_b^{\text{stat}} \oplus \delta_b^{\text{eff}})^2 + \rho_{bb'} \delta_b^{\text{corr}} \delta_{b'}^{\text{corr}}, \quad (24)$$

where $b, b' = 1, \dots, N_{\text{bin}}$ is the bin index, $N_{\text{bin}} = 12$ is the number of bins, I is the identity matrix, $\delta_b^{\text{stat/eff/corr}}$ is the absolute statistical, efficiency, and correlated uncertainties at the b th bin, respectively, given by

$$\delta_b^{\text{stat}} = \frac{1}{\sqrt{\sigma_{\text{SM},b} \mathcal{L}}} \times \sigma_{\text{SM},b}, \quad \delta_b^{\text{eff}} = 5\% \times \sigma_{\text{SM},b}, \quad \delta_b^{\text{corr}} = 1.7\% \times \sigma_{\text{SM},b}, \quad (25)$$

and \oplus indicates sum in quadrature. We assume $\rho_{bb'} = 1$ for all bins. On the theoretical side, we have fully correlated PDF uncertainties, as well as uncorrelated 3-point scale variations. The PDF uncertainty matrix for Hessian sets is given by

$$\mathcal{E}_{bb'}^{\text{pdf}} = \frac{1}{4} \sum_{m=1}^{N_{\text{pdf}}/2} (\mathcal{O}_{2m} - \mathcal{O}_{2m-1})_b (\mathcal{O}_{2m} - \mathcal{O}_{2m-1})_{b'}, \quad (26)$$

and the scale variations are defined as

$$\mathcal{E}_{bb'}^{\text{scale}} = I_{bb'} \max \left\{ \left| \mathcal{O}_b^{(f_R, f_F)} - \mathcal{O}_b^{(1,1)} \right|^2 \right\} \quad (27)$$

where N_{pdf} is the number of PDF members in a given set and we consider $(f_R, f_F) = \{(0.5, 0.5), (1, 1), (2, 2)\}$. We note that the model function is taken without theoretical uncertainties. PDF and scale variations are defined at the SM baseline and propagated consistently. Assigning them separately to SMEFT corrections would double count and introduce spurious C -dependence in the uncertainty matrix.

The pseudodata is generated by smearing SM values around using the experimental uncertainties:

$$\mathcal{O}_b = \mathcal{O}_{\text{SM},b} + r_b (\delta_b^{\text{stat}} \oplus \delta_b^{\text{eff}}) + r' \delta_b^{\text{corr}}, \quad (28)$$

where $r_b, r' \in \mathcal{N}(0, 1)$ unit normal variates. The correlated uncertainty is introduced with the same factor so that all the bins feel the shift by the same amount. For our analysis to make sense statistically, we need to run multiple pseudoexperiments, hence it is now appropriate to introduce the subscript e so we have χ_e^2 denoting the chi-squared function of the e th pseudoexperiment. We obtain the best-fit values $\bar{\mathbf{C}}_e$ by setting the gradient equal to zero in the parameter space,

$$\nabla \chi_e^2(\bar{\mathbf{C}}_e) = \mathbf{0}, \quad (29)$$

and the Fisher information matrix is just the Hessian evaluated at the best-fit values,

$$\mathcal{F}_e = \nabla \nabla \chi_e^2(\bar{\mathbf{C}}_e). \quad (30)$$

The best-fit values of SMEFT parameters averaged over pseudoexperiments is given by

$$\bar{\mathbf{C}} = \left(\sum_{e=1}^{N_{\text{exp}}} \mathcal{F}_e \right)^{-1} \sum_{e=1}^{N_{\text{exp}}} \mathcal{F}_e \bar{\mathbf{C}}_e, \quad (31)$$

and the Fisher matrix averaged over the pseudoexperiments by

$$\mathcal{F} = \frac{1}{N_{\text{exp}}} \sum_{e=1}^{N_{\text{exp}}} \mathcal{F}_e, \quad (32)$$

where N_{exp} is the number of pseudoexperiments. We find that with $N_{\text{exp}} = 10^4$ pseudoexperiments, the fits stabilize and we attain reliable statistics. For the combined fit of Run II+III, we assume they are independent so we simply add the individual Fisher matrices, $\mathcal{F}_{\text{II+III}} = \mathcal{F}_{\text{II}} + \mathcal{F}_{\text{III}}$.

Before presenting the fit results, we summarize the error budget entering our fits, namely the individual contributions to the diagonal entries of the total uncertainty matrix. In Figs. 7 and 8, we show for each bin the SM predictions at LO, NLO, and aNNLO together with the corresponding uncertainty components in absolute terms on the left panels, as well as the same components relative to the SM prediction expressed in units of percent on the right for Run II and Run III configurations, respectively. The black line is for the SM prediction, red for statistical uncertainties, blue for the assumed 5% global uncorrelated uncertainty, magenta for the assumed 1.7% correlated luminosity uncertainty, orange for 3-point scale variations, and green for PDF uncertainties. The dotted line is for LO, dashed for NLO, and solid for aNNLO.

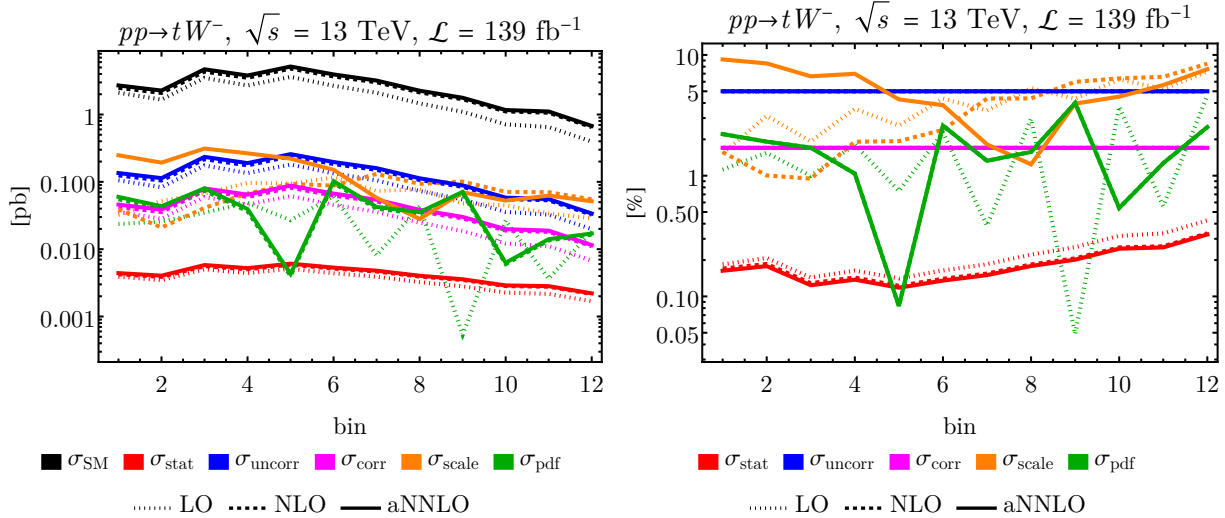


FIG. 7. The error budget for the Run II configuration with $\sqrt{s} = 13$ TeV and $\mathcal{L} = 139 \text{ fb}^{-1}$, showing the LO, NLO, and aNNLO SM predictions and their uncertainty components in absolute terms (left) and relative to the SM in units of percent (right) for each bin.

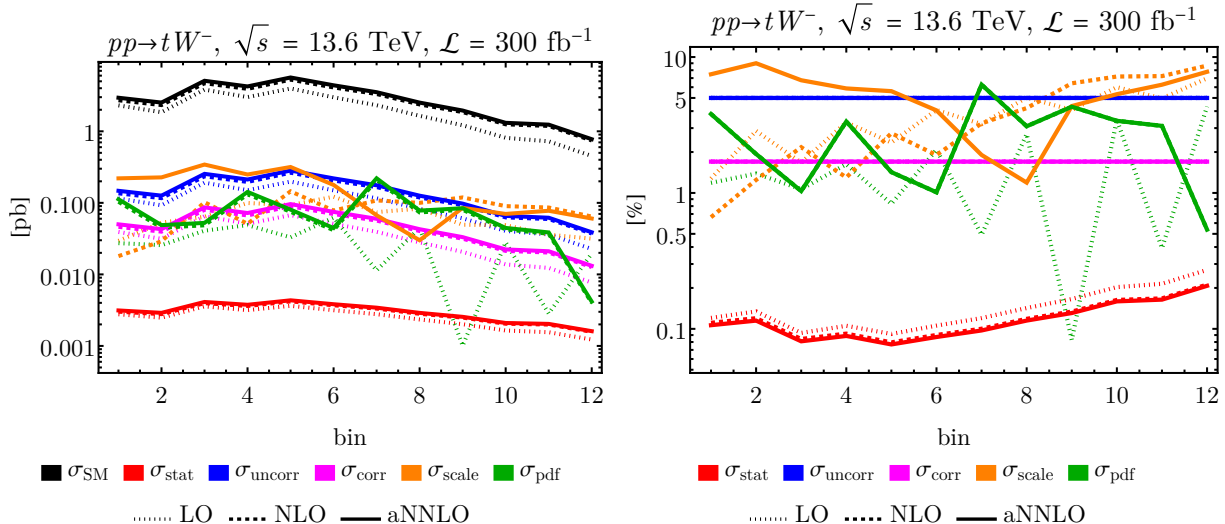


FIG. 8. The same as Fig. 7 but for the Run III configuration with $\sqrt{s} = 13.6$ TeV and $\mathcal{L} = 300 \text{ fb}^{-1}$.

We find that the dominant uncertainty is set by a competition between the 3-point scale variation and the assumed global uncorrelated uncertainty. The next largest contributions come from the PDF variations and the correlated luminosity uncertainty, which are comparable in size. By contrast, the statistical uncertainties play the weakest role.

V. SMEFT FIT RESULTS

In this section, we present the SMEFT fit results. First, we report the Fisher information matrices for the Run II and Run III configurations for the linear and quadratic fits at LO, NLO, and aNNLO:

$$\mathcal{F}_{\text{II}}^{\text{LO,linear}} = \begin{pmatrix} 16.24 & -19.02 & 13.46 \\ -19.02 & 22.32 & -15.78 \\ 13.46 & -15.78 & 11.22 \end{pmatrix}, \quad (33)$$

$$\mathcal{F}_{\text{III}}^{\text{LO,linear}} = \begin{pmatrix} 16.92 & -19.75 & 13.99 \\ -19.75 & 23.08 & -16.35 \\ 13.99 & -16.35 & 11.64 \end{pmatrix}, \quad (34)$$

$$\mathcal{F}_{\text{II}}^{\text{LO,quadratic}} = \begin{pmatrix} 21.34 & -20.21 & 13.49 \\ -20.21 & 25.94 & -15.22 \\ 13.49 & -15.22 & 11.12 \end{pmatrix}, \quad (35)$$

$$\mathcal{F}_{\text{III}}^{\text{LO,quadratic}} = \begin{pmatrix} 22.15 & -21.00 & 13.95 \\ -21.00 & 27.57 & -16.07 \\ 13.95 & -16.07 & 11.56 \end{pmatrix}, \quad (36)$$

$$\mathcal{F}_{\text{II}}^{\text{NLO,linear}} = \begin{pmatrix} 13.07 & -15.97 & 10.92 \\ -15.97 & 19.74 & -13.53 \\ 10.92 & -13.53 & 9.316 \end{pmatrix}, \quad (37)$$

$$\mathcal{F}_{\text{III}}^{\text{NLO,linear}} = \begin{pmatrix} 9.579 & -11.63 & 8.418 \\ -11.63 & 14.23 & -10.26 \\ 8.418 & -10.26 & 7.551 \end{pmatrix}, \quad (38)$$

$$\mathcal{F}_{\text{II}}^{\text{NLO,quadratic}} = \begin{pmatrix} 18.28 & -15.21 & 10.30 \\ -15.21 & 25.14 & -13.38 \\ 10.30 & -13.38 & 9.674 \end{pmatrix}, \quad (39)$$

$$\mathcal{F}_{\text{III}}^{\text{NLO,quadratic}} = \begin{pmatrix} 14.57 & -12.24 & 7.425 \\ -12.24 & 18.42 & -10.59 \\ 7.425 & -10.59 & 8.228 \end{pmatrix}, \quad (40)$$

$$\mathcal{F}_{\text{II}}^{\text{aNNLO, linear}} = \begin{pmatrix} 11.68 & -14.21 & 9.842 \\ -14.21 & 17.47 & -12.11 \\ 9.842 & -12.11 & 8.425 \end{pmatrix}, \quad (41)$$

$$\mathcal{F}_{\text{III}}^{\text{aNNLO, linear}} = \begin{pmatrix} 7.368 & -9.042 & 6.543 \\ -9.042 & 11.18 & -8.069 \\ 6.543 & -8.069 & 5.911 \end{pmatrix}, \quad (42)$$

$$\mathcal{F}_{\text{II}}^{\text{aNNLO, quadratic}} = \begin{pmatrix} 15.74 & -13.31 & 9.343 \\ -13.31 & 21.50 & -11.79 \\ 9.343 & -11.79 & 8.864 \end{pmatrix}, \quad (43)$$

$$\mathcal{F}_{\text{III}}^{\text{aNNLO, quadratic}} = \begin{pmatrix} 11.63 & -9.680 & 5.712 \\ -9.680 & 15.12 & -8.472 \\ 5.712 & -8.472 & 6.671 \end{pmatrix}. \quad (44)$$

We emphasize that our results are presented for $pp \rightarrow tW^-$ throughout. The charge-conjugate channel $pp \rightarrow \bar{t}W^+$ yields essentially the same kinematic dependence and nearly identical rates, so its impact on the statistical sensitivity is, to an excellent approximation, an overall doubling of the information content. Consequently, if both channels are included with identical binning and uncertainty treatment, one may approximate the combined constraints by rescaling the Fisher information matrix as $F_{tW^- + \bar{t}W^+} \simeq 2F_{tW^-}$, which implies the corresponding marginalized uncertainties shrink by a factor $1/\sqrt{2}$. We have checked that this approximation is sufficient at the level of precision targeted in this work.

Next, we present 95% CL bounds on C_{tG} , C_{tW} , and C_p for linear and quadratic SMEFT fits. Fig. 9 shows the nonmarginalized and marginalized bounds for the linear fit, and Fig. 10 shows the same for the quadratic fit. Here, the band of colors on the left is for C_{tG} , center for C_{tW} , and right for C_p . The black color family is for LO, red for NLO, and blue for aNNLO. The darkest shade of each color family is for Run II, middle for Run III, and the lightest for the combined fit Run II and Run III.

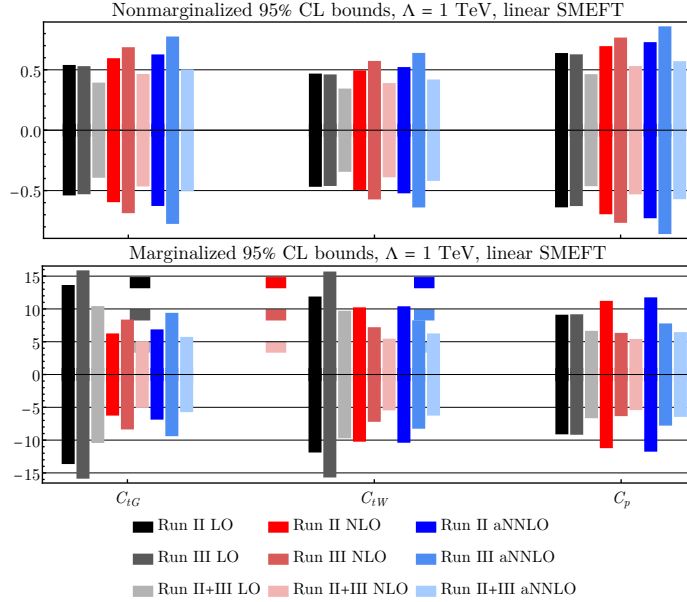


FIG. 9. Nonmarginalized (top) and marginalized (bottom) 95% CL bounds for the linear fit for Run II, Run III, and Run II+III at LO, NLO, and aNNLO.

At linear order in the Wilson coefficients, the nonmarginalized bounds are at the level of $\mathcal{O}(0.1)$, while the marginalized bounds degrade to $\mathcal{O}(10)$. This large weakening indicates strong correlations in the multi-parameter fit. The Run II and Run III bounds are comparable in size because we use the same bins and the collider energy is slightly increased, so the combined Run II+III fit yields only a modest improvement over the individual results.

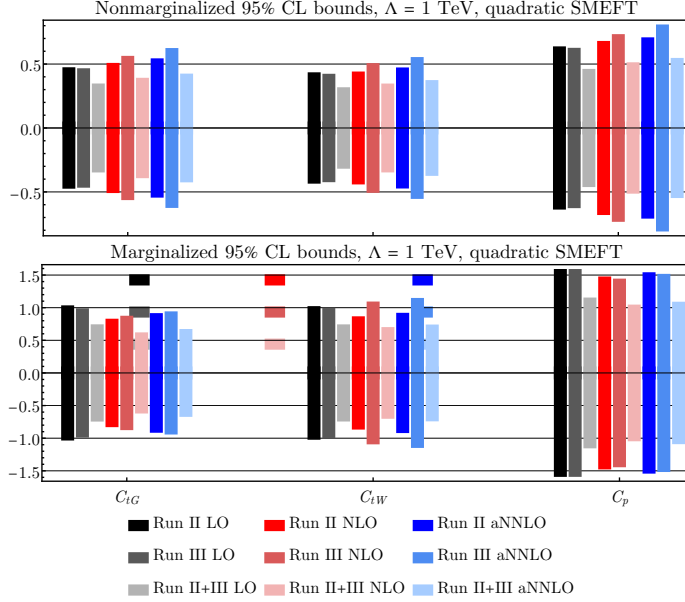


FIG. 10. The same as Fig. 9 but for the quadratic fit.

At quadratic order, the nonmarginalized bounds are comparable to those from the linear fit, while the difference becomes significant after marginalization. The marginalized quadratic bounds are about an order of magnitude stronger than the marginalized linear bounds, indicating that including squared dimension-6 terms improves the constraining power of the fit. This improvement should be interpreted with care, since quadratic dimension-6 effects are parametrically of the same order as linear dimension-8 contributions, and a consistent assessment would require including the dimension-8 operators.

Next, we quote the corresponding effective scales defined as $\Lambda/\sqrt{\Delta C_k}$ using the 95% CL bounds. Fig. 11 shows the nonmarginalized and marginalized effective scales for the linear fit, and Fig. 12 shows the same for the quadratic fit. The organization of the plots is the same as the bounds.

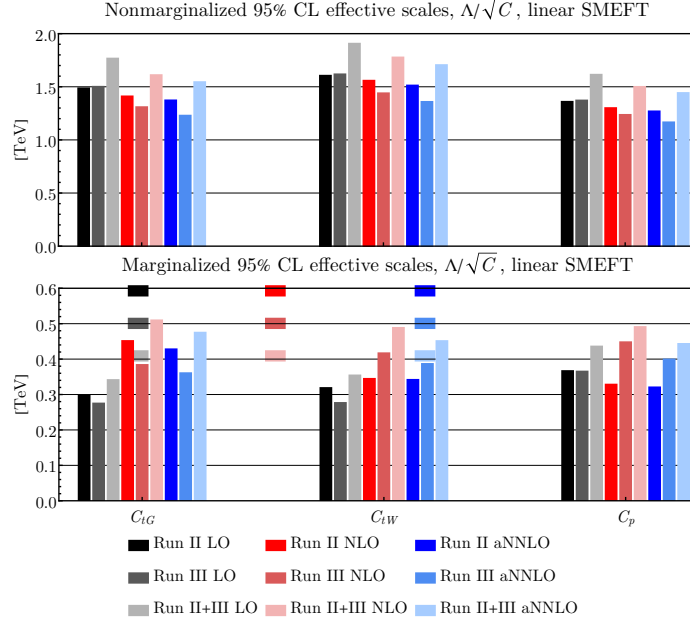


FIG. 11. Nonmarginalized (top) and marginalized (marginalized) effective scales $\Lambda/\sqrt{\Delta C_k}$ for the linear fit for Run II, Run III, and Run II+III at LO, NLO, and aNNLO.

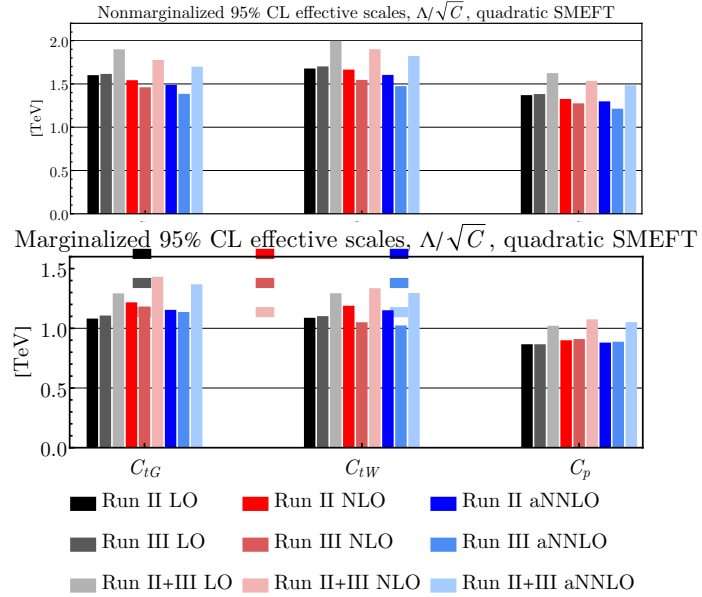


FIG. 12. The same as Fig. 11 but for the quadratic fit.

At linear order, the nonmarginalized bounds correspond to effective scales up to about 2 TeV, while the marginalized bounds reduce this reach to roughly 0.5 TeV. For the quadratic fit, the nonmarginalized reach is again around 2 TeV, and the marginalized reach increases

to nearly 1.5 TeV. Since the characteristic scale of the process is set by the top quark mass, these numbers suggest that the EFT expansion parameter m_t/Λ is better behaved once the squared dimension-6 terms are included. This provides additional motivation to extend the analysis in the future by incorporating dimension-8 effects for a more complete EFT description.

We next show correlation matrices for the marginalized fits. Fig. 13 shows the Run II correlation matrices, Fig. 14 shows the Run III correlation matrices, and Fig. 15 shows the Run II+III correlation matrices.

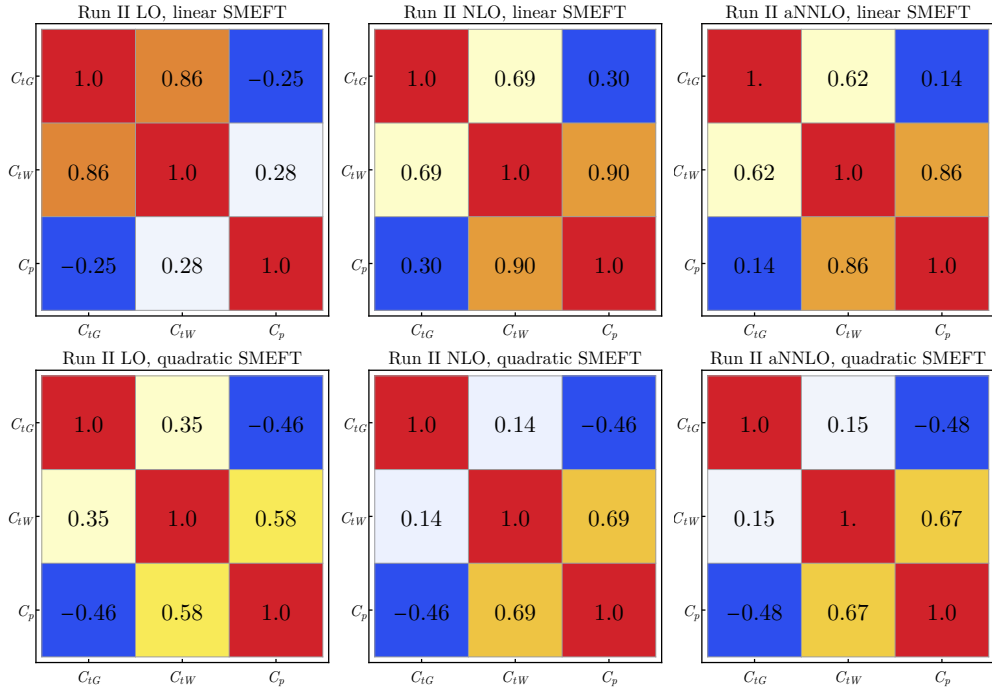


FIG. 13. Correlation matrices for the marginalized linear (top) and quadratic (bottom) fits for Run II at LO (left), NLO (center), and aNNLO (right).

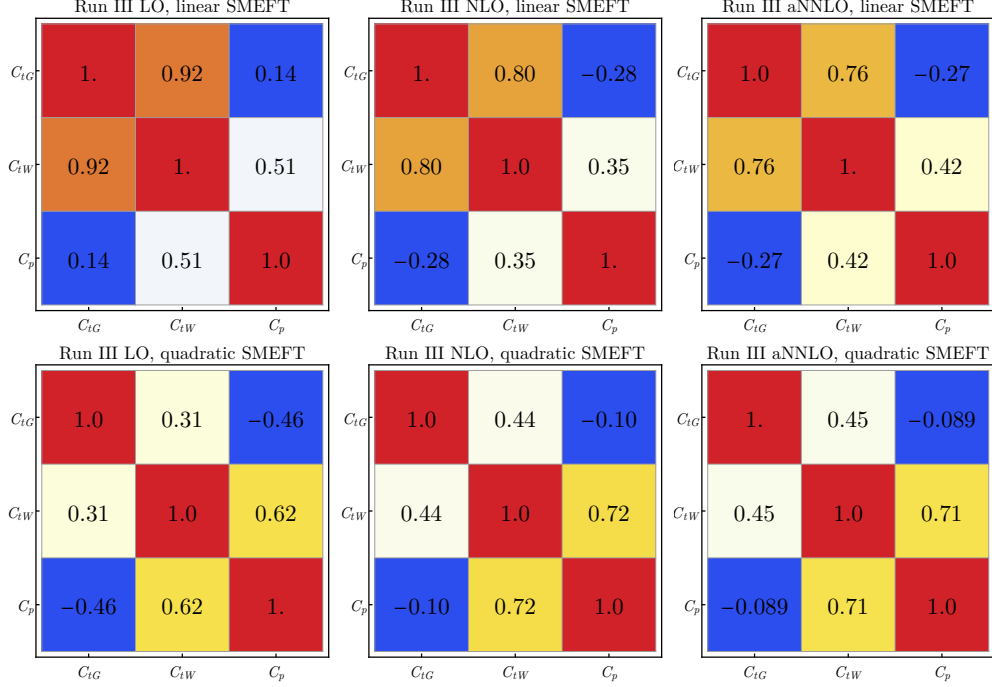


FIG. 14. The same as Fig. 13 but for Run III.

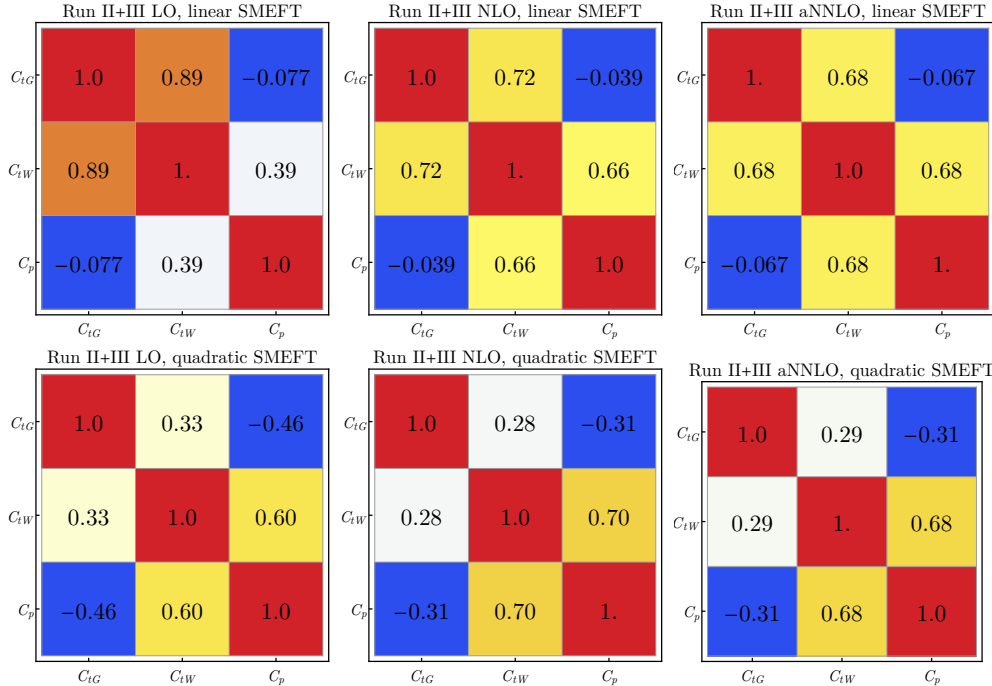


FIG. 15. The same as Fig. 13 but for Run II+III.

The correlation matrices for the 3-parameter fits indicate sizable correlations among the SMEFT coefficients, consistent with the strong degradation observed upon marginalization.

At the same time, the matrices remain well behaved, showing that the fits are not dominated by exact flat directions. Moving between perturbative orders can change both the magnitude and the pattern of these correlations, reflecting the modified kinematic dependence and normalization of the SMEFT contributions at each order, but it does not qualitatively alter the structure of the fit. Since we use the same binning for the Run II and Run III configurations, the overall correlation patterns are expected to be similar, with differences driven primarily by the higher collider energy. In particular, the slight strengthening of specific correlations in Run III can be understood as a consequence of the increased weight of higher partonic center-of-mass energies in the convolution, which changes the relative importance of the underlying kinematic structures in the amplitude.

We now show selected confidence ellipses. The complete set of ellipses is provided in Appendix A. Fig. 16 compares the nonmarginalized and marginalized constraints in the (C_{tG}, C_{tW}) parameter subspace for Run II at LO, NLO, and aNNLO. In this figure, the black curve denotes the confidence ellipse at LO, red at NLO, and blue at aNNLO. Here, nonmarginalized refers to fits in which only two Wilson coefficients are allowed to vary at a time, with the remaining coefficient set to zero, while marginalized refers to the full 3-parameter fit projected onto the chosen two-dimensional subspace. In the parameter subspace spanned by C_{tG} and C_{tW} , the nonmarginalized contours exhibit a pronounced correlation, reflecting the similar imprint of these operators in this channel. After marginalization, the projected constraints take the form of more regular ellipses, indicating that the global fit remains well defined once all coefficients are floated simultaneously. The resulting constraints on C_{tG} and C_{tW} are comparable in size between the 2-parameter and 3-parameter fits, suggesting that the inclusion of the third coefficient primarily stabilizes the fit by lifting potential degeneracies rather than substantially reshaping the allowed region in this projection.

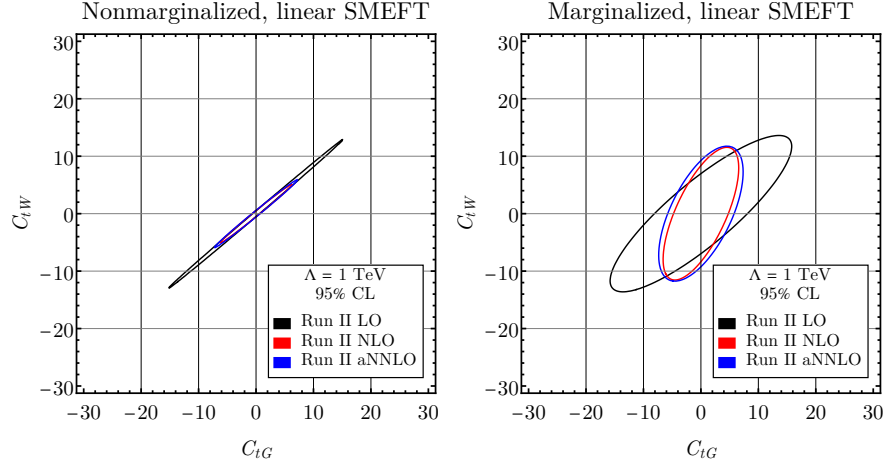


FIG. 16. Nonmarginalized (left) and marginalized (right) confidence ellipses in the parameter subspace (C_{tG}, C_{tW}) for the linear fit for Run II at LO, NLO, and aNNLO.

Fig. 17 compares the marginalized linear and quadratic constraints in the parameter subspace (C_{tG}, C_p) for the combined Run II+III fit. The organization of the plots is identical to Fig. 16. Focusing on the comparison between the linear and quadratic fits, we find that the marginalized linear confidence ellipse shows only mild correlations between C_{tG} and C_p , but the overall extent of the allowed region remains relatively broad. Once the quadratic dimension-6 terms are included, the constraint tightens substantially, in line with the order-of-magnitude improvement observed in the marginalized bounds. This sensitivity to quadratic dimension-6 effects provides further motivation for extending the EFT description in future work by incorporating dimension-8 operators.

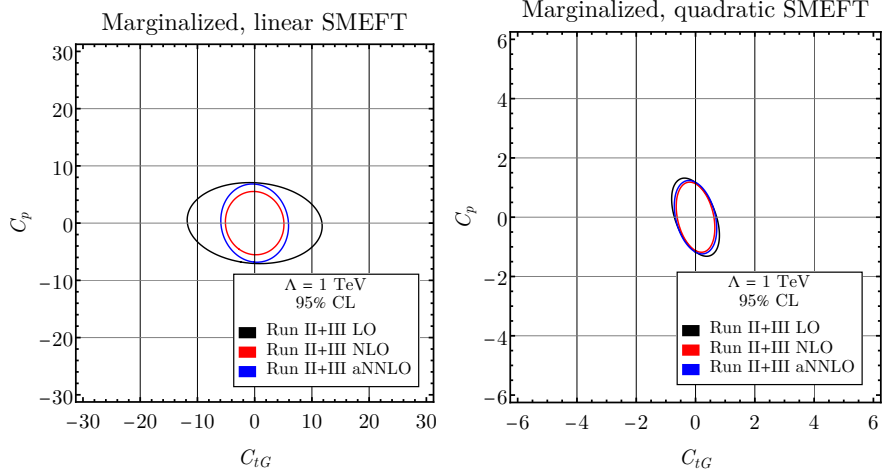


FIG. 17. Marginalized confidence ellipses in the parameter subspace (C_{tG}, C_p) for the combined Run II+III fit, comparing the linear (left) and quadratic (right) fits at LO, NLO, and aNNLO.

Fig. 18 shows the effect of combining Run II and Run III in the parameter subspace (C_{tW}, C_p) for the quadratic fit. The plot layout follows that of Fig. 16, with the same ordering in perturbative accuracy. Since we use the same binning and the same assumptions for the uncorrelated and correlated experimental uncertainties in Run II and Run III, and since the increase in the collider energy is modest, the two runs provide very similar constraint contours. The main difference between the configurations is the larger integrated luminosity in Run III, but because the fits are not statistics-limited, the combined Run II+III ellipses are only moderately tighter than the individual Run II result, at the level expected from effectively adding an additional, comparable dataset. A more pronounced gain would likely require additional differential information, such as finer binning or extended kinematic coverage in Run III, which would come at increased computational cost in the fixed order predictions and their uncertainty evaluation.

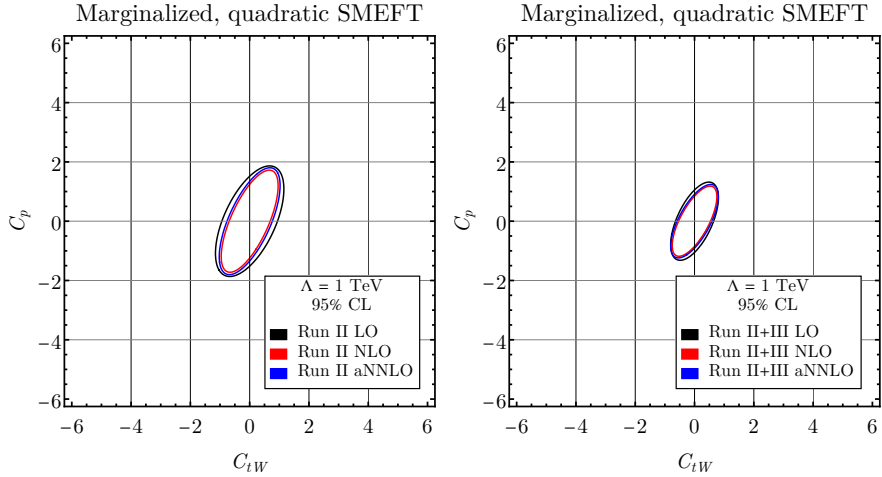


FIG. 18. Marginalized confidence ellipses in the parameter subspace (C_{tW}, C_p) for the quadratic fit at LO, NLO, and aNNLO, comparing Run II (left) and the combined Run II+III (right) fits.

A final point is that C_p represents a specific linear combination of three Wilson coefficients, $C_{\varphi Q}^{(3)}$, $C_{\ell\ell}$, and $C_{\varphi\ell}^{(3)}$. As a result, the tW analysis alone cannot disentangle these three directions, and there will remain an intrinsic degeneracy associated with resolving the individual underlying operators unless additional observables or complementary processes are included.

Before we end this section, we compare our fit results with those in the literature in Table V and in the parameter subspace spanned by C_{tG} and C_{tW} in Fig. 19. The results summarized here are not strictly equivalent in scope. Our fit is performed in the tW channel using differential information and a three-parameter SMEFT model, and is therefore sensitive to degeneracies internal to this process. By contrast, the HEPfit global analysis [116] combines a broad set of legacy and LHC measurements (including electroweak precision observables and multiple collider processes) in a 22-parameter SMEFT fit, which helps break correlations among operators through complementary sensitivity. Similarly, the SMEFiT global fit [117] incorporates a larger operator set together with a wide collection of datasets spanning precision electroweak, Higgs, top, and diboson measurements, such that its constraints reflect the combined information content of many channels. Finally, the single-parameter constraint labeled “ $t\bar{t}$ cross section” [55] is obtained from a fit to an inclusive $t\bar{t}$ cross-section measurement alone [118, 119], effectively a single experimental input, and should be interpreted as a dedicated one-operator extraction rather than a global

analysis.

With these differences in mind, Table V indicates that our extracted one-dimensional limits on C_{tG} and C_{tW} are weaker than those obtained in recent global fits, corresponding to smaller effective scales. This trend is expected; namely, global analyses leverage multiple processes with distinct operator dependence, thereby reducing degeneracies between SMEFT corrections characterized by C_{tG} and C_{tW} and typically yielding small correlations in the (C_{tG}, C_{tW}) subspace after combining complementary inputs. In contrast, a channel-restricted fit in tW can exhibit stronger internal correlations once experimental and theoretical systematics are included, since different operators may induce similar deformations in the available distributions. It is also instructive to compare to the dedicated one-parameter extraction from the inclusive $t\bar{t}$ cross section, which yields a comparatively strong constraint on C_{tG} despite using only a single observable; this reflects the high intrinsic sensitivity of inclusive $t\bar{t}$ production to the chromomagnetic dipole operator.

TABLE V. Comparison of representative constraints on the top dipole operators C_{tG} and C_{tW} from this work and selected recent analyses in the literature. We also report the corresponding effective scales. All coefficients are given in the SMEFT@NLO convention.

	SMEFT order	Accuracy	Number of parameters	C_{tG}	$\Lambda_{\text{eff}}(tG)$ [TeV]	C_{tW}	$\Lambda_{\text{eff}}(tW)$ [TeV]
This work	Quadratic	aNNLO	3	0.60	1.3	0.60	1.3
Global fit with HEPfit [116]	Linear	NLO	22	0.32	1.8	0.26	2.0
Global fit with SMEFiT [117]	Quadratic	NLO	50	0.081	3.5	0.16	2.5
$t\bar{t}$ cross section [55]	Quadratic	aNNLO	1	0.25	2.0	–	–

The corresponding two-dimensional comparison is shown in Fig. 19. We display the 95% CL contours in the parameter subspace spanned by C_{tG} and C_{tW} at $\Lambda = 1$ TeV. The entries “This work”, “HEPfit”, and “SMEFiT” are the same as in Table V. The HEPfit and SMEFiT contours are reported with negligible C_{tG} - C_{tW} correlation in their summaries; in particular, HEPfit (SMEFiT) sets $\rho = 0$ whenever $|\rho| < 0.05$ ($|\rho| < 0.2$), and we adopt the same convention in the figure. Although our confidence ellipse is broader and exhibits a sizable correlation, all three ellipses lie within a compact region of the parameter plane, indicating that our tW -based determination is broadly comparable in scale to existing global constraints while providing a complementary, process-specific result at aNNLO accuracy.

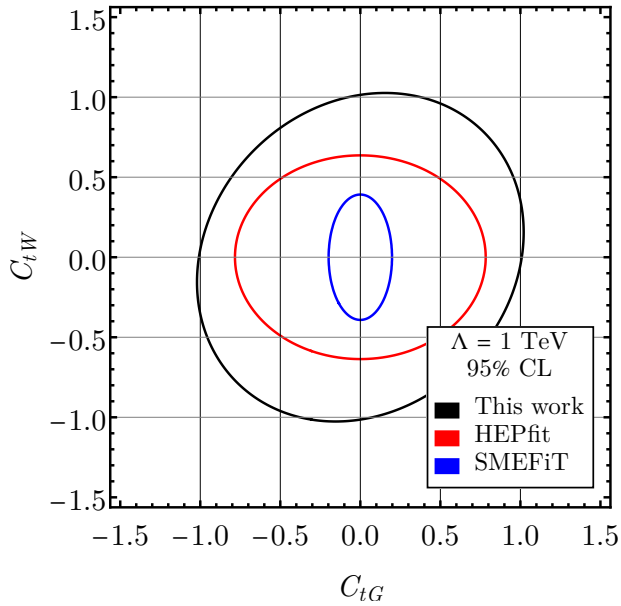


FIG. 19. Comparison of the 95% CL constraints in the parameter subspace (C_{tG}, C_{tW}) from this work and the global analyses of HEPfit and SMEFiT, shown in the SMEFT@NLO convention for $\Lambda = 1$ TeV.

VI. CONCLUSION

In this work, we studied $pp \rightarrow tW^-$ production at the LHC within the dimension-6 SMEFT and presented predictions at LO, NLO QCD, and aNNLO QCD accuracy, with the NLO calculation defined using a diagram-removal prescription to avoid overlap with resonant $t\bar{t}$ contributions. We analyzed double differential top quark distributions in transverse momentum and rapidity and provided a complete account of the uncertainty budget entering our fits.

We performed linear and quadratic SMEFT fits to C_{tG} , C_{tW} , and C_p for Run II and Run III configurations. At linear order in SMEFT parameters, the nonmarginalized 95% CL bounds are $\mathcal{O}(0.1)$, while the marginalized bounds weaken to $\mathcal{O}(10)$, reflecting strong correlations in the 3-parameter fit; Run II and Run III constraints are similar, so the combined Run II+III fit improves only modestly. Including quadratic dimension-6 terms leaves the nonmarginalized bounds at a similar level but strengthens the marginalized bounds by about an order of magnitude relative to the marginalized linear fit. This behavior is also visible in the effective scale reach. The nonmarginalized fits probe scales up to about 2 TeV, while the

marginalized reach is roughly 0.5 TeV in the linear fit and around 1.5 TeV in the quadratic fit. These improvements motivate a more complete EFT treatment, since the quadratic dimension-6 effects are parametrically comparable to linear dimension-8 contributions, and a consistent interpretation would benefit from including dimension-8 operators. In addition, C_p is a fixed linear combination of $C_{\varphi Q}^{(3)}$, $C_{\ell\ell}$, and $C_{\varphi\ell}^{(3)}$, so resolving the underlying operator directions will require additional observables or complementary processes beyond tW alone.

Finally, we compared our constraints on C_{tG} and C_{tW} to recent results in the literature, including global SMEFT fits and a dedicated one-parameter extraction from the inclusive $t\bar{t}$ cross section. While global analyses typically yield stronger one-dimensional limits by combining complementary information from many channels, our tW -based determination is broadly comparable in scale in the parameter subspace (C_{tG}, C_{tW}) and provides a complementary, process-specific constraint at aNNLO accuracy.

Acknowledgments: This material is based upon work supported by the National Science Foundation under Grant No. PHY 2412071. K\$ is supported by the Kennesaw State University Office of Research Postdoctoral Fellowship Program. This work was supported in part by research computing resources and technical expertise via a partnership between Kennesaw State University’s Office of the Vice President for Research and the Office of the CIO and Vice President for Information Technology.

Appendix A: Complete set of confidence ellipses

In this section, we present the complete set of confidence ellipses for the SMEFT fit results in Figs. 20–28.

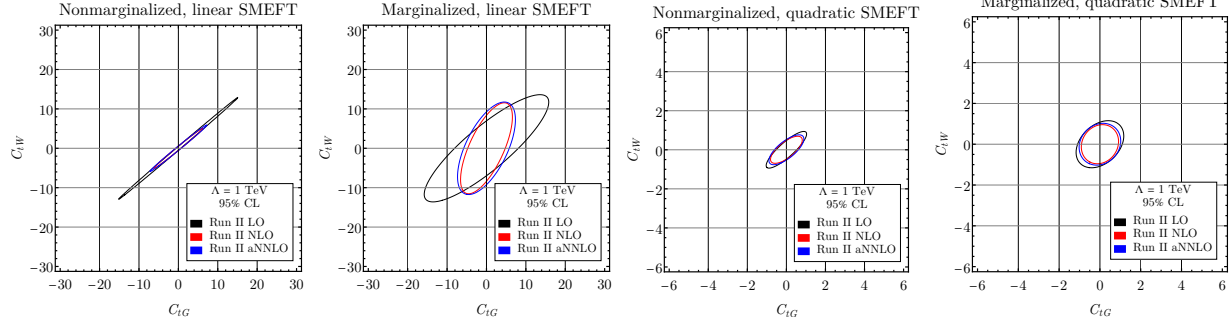


FIG. 20. Confidence ellipses in the parameter subspace (C_{tG}, C_{tW}) for Run II comparing the nonmarginalized linear fit (first), marginalized linear fit (second), nonmarginalized quadratic fit (third), and marginalized quadratic fit (fourth), each shown at LO, NLO, and aNNLO.

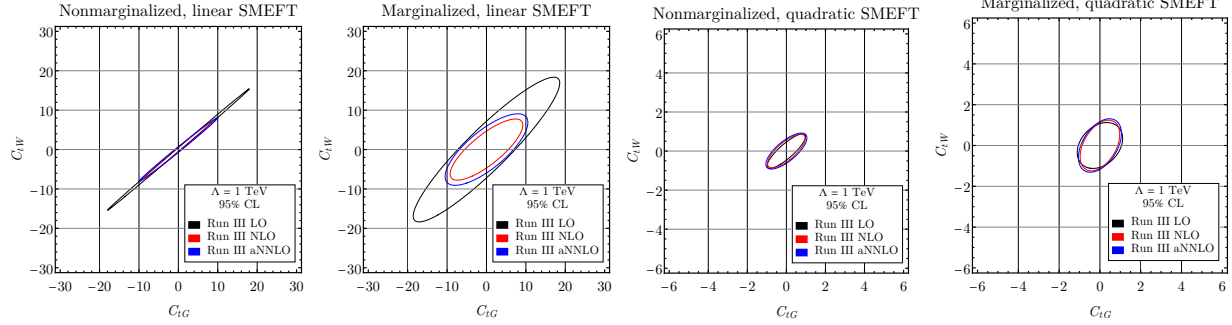


FIG. 21. The same as Fig. 20 but for Run III.

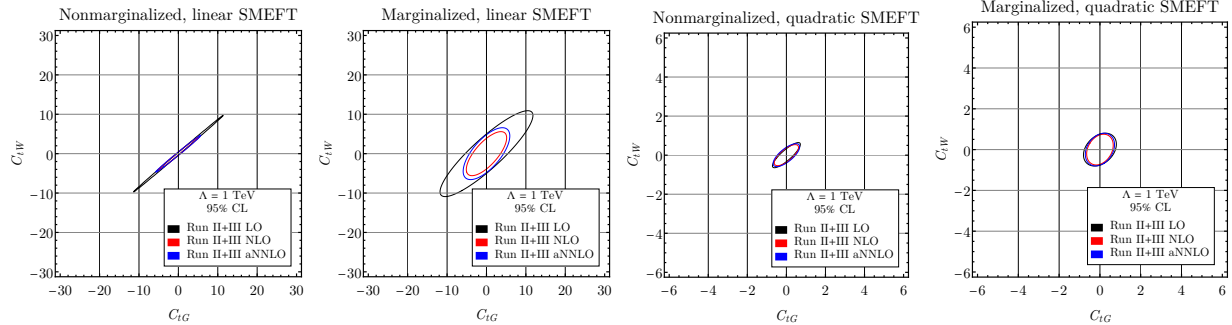
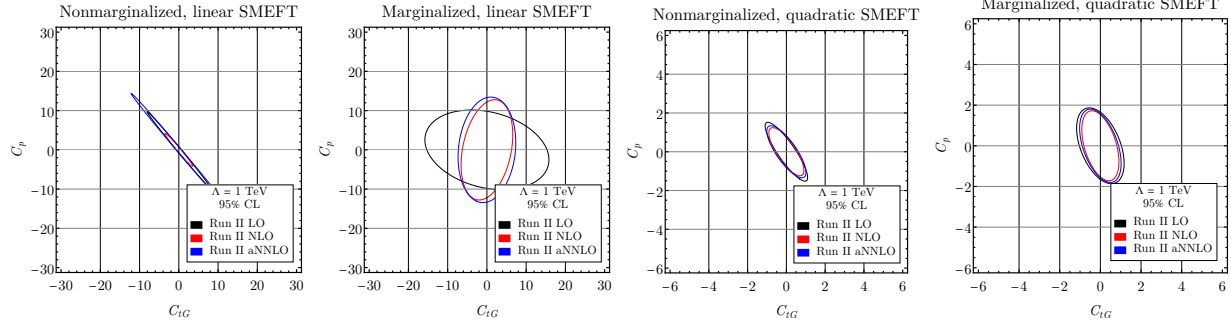
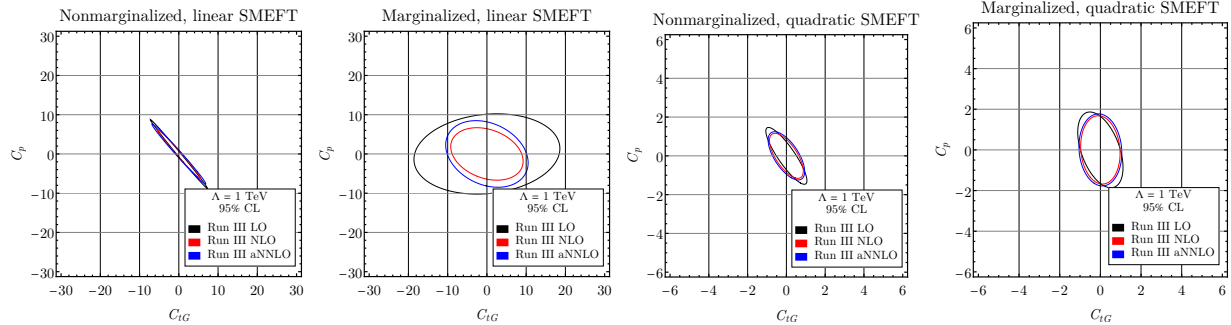
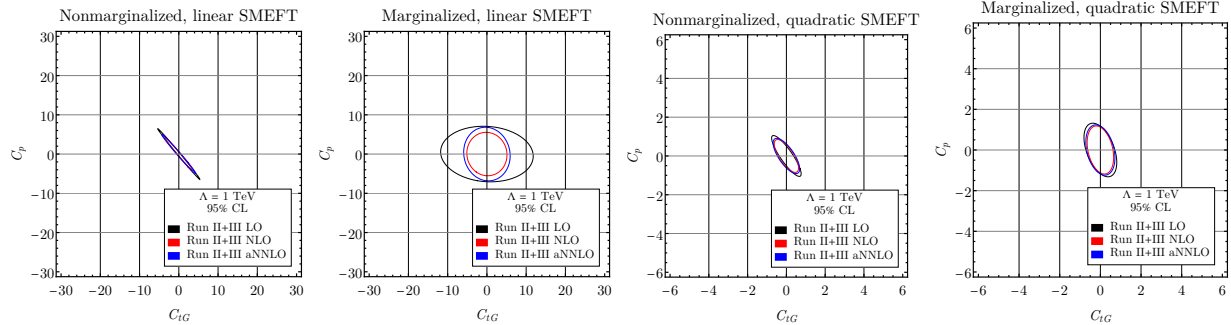
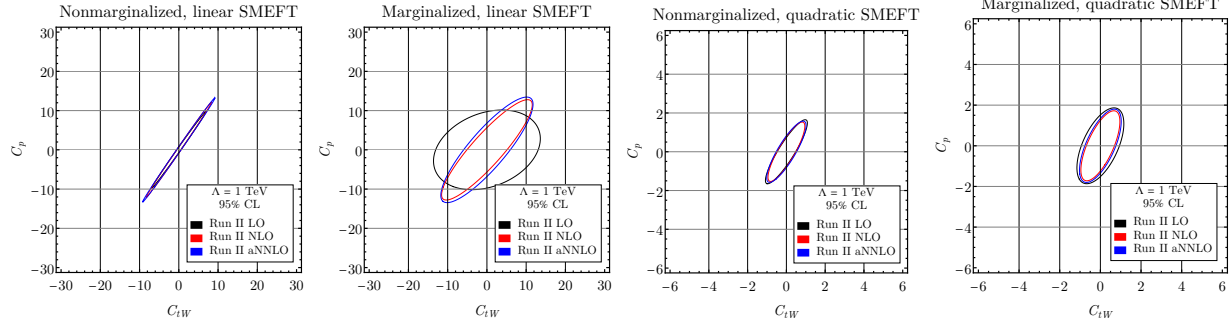
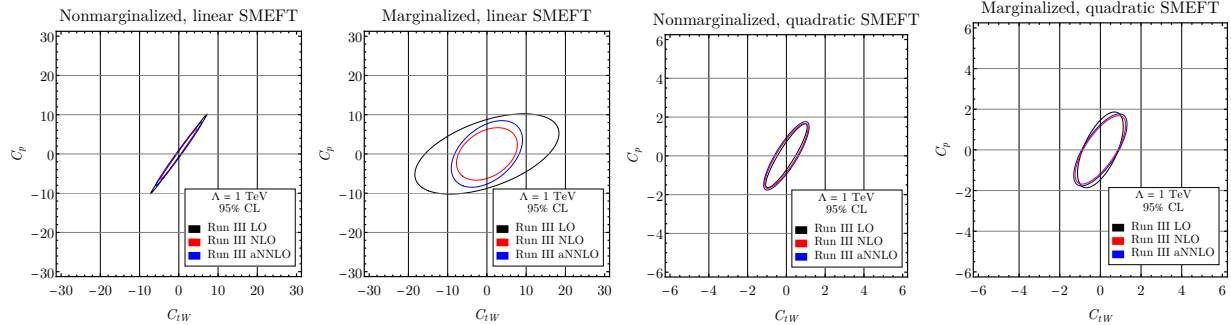
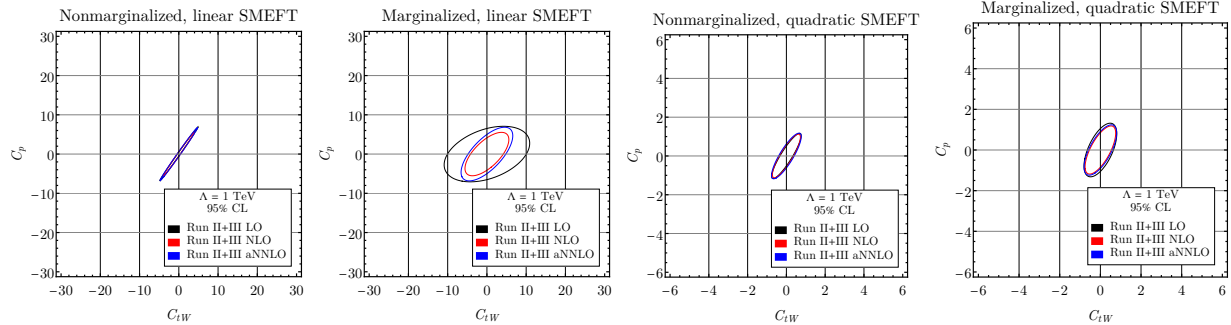


FIG. 22. The same as Fig. 20 but for Run II+III.

FIG. 23. The same as Fig. 20 but for (C_{tG}, C_p) .FIG. 24. The same as Fig. 21 but for (C_{tG}, C_p) .FIG. 25. The same as Fig. 22 but for (C_{tG}, C_p) .

FIG. 26. The same as Fig. 20 but for (C_{tW}, C_p) .FIG. 27. The same as Fig. 21 but for (C_{tW}, C_p) .FIG. 28. The same as Fig. 22 but for (C_{tW}, C_p) .

[1] B. Grzadkowski, M. Iskrzynski, M. Misiak, and J. Rosiek, Dimension-Six Terms in the Standard Model Lagrangian, *JHEP* **10**, 085, arXiv:1008.4884 [hep-ph].

- [2] A. Pomarol and F. Riva, Towards the Ultimate SM Fit to Close in on Higgs Physics, *JHEP* **01**, 151, arXiv:1308.2803 [hep-ph].
- [3] A. Falkowski, Effective field theory approach to LHC Higgs data, *Pramana* **87**, 39 (2016), arXiv:1505.00046 [hep-ph].
- [4] C. W. Murphy, Dimension-8 operators in the Standard Model Effective Field Theory, *JHEP* **10**, 174, arXiv:2005.00059 [hep-ph].
- [5] H.-L. Li, Z. Ren, J. Shu, M.-L. Xiao, J.-H. Yu, and Y.-H. Zheng, Complete set of dimension-eight operators in the standard model effective field theory, *Phys. Rev. D* **104**, 015026 (2021), arXiv:2005.00008 [hep-ph].
- [6] R. V. Harlander, T. Kempkens, and M. C. Schaaf, Standard model effective field theory up to mass dimension 12, *Phys. Rev. D* **108**, 055020 (2023), arXiv:2305.06832 [hep-ph].
- [7] B. Henning, X. Lu, T. Melia, and H. Murayama, Hilbert series and operator bases with derivatives in effective field theories, *Commun. Math. Phys.* **347**, 363 (2016), arXiv:1507.07240 [hep-th].
- [8] B. Henning, X. Lu, T. Melia, and H. Murayama, 2, 84, 30, 993, 560, 15456, 11962, 261485, ...: Higher dimension operators in the SM EFT, *JHEP* **08**, 016, [Erratum: *JHEP* 09, 019 (2019)], arXiv:1512.03433 [hep-ph].
- [9] L. Graf, B. Henning, X. Lu, T. Melia, and H. Murayama, 2, 12, 117, 1959, 45171, 1170086, ...: a Hilbert series for the QCD chiral Lagrangian, *JHEP* **01**, 142, arXiv:2009.01239 [hep-ph].
- [10] L. Gráf, B. Henning, X. Lu, T. Melia, and H. Murayama, Hilbert series, the Higgs mechanism, and HEFT, *JHEP* **02**, 064, arXiv:2211.06275 [hep-ph].
- [11] A. Dedes, W. Mąterkowska, M. Paraskevas, J. Rosiek, and K. Suxho, Feynman rules for the Standard Model Effective Field Theory in R_ξ -gauges, *JHEP* **06**, 143, arXiv:1704.03888 [hep-ph].
- [12] A. Dedes, M. Paraskevas, J. Rosiek, K. Suxho, and L. Trifyllis, SmeftFR – Feynman rules generator for the Standard Model Effective Field Theory, *Comput. Phys. Commun.* **247**, 106931 (2020), arXiv:1904.03204 [hep-ph].
- [13] A. Dedes, J. Rosiek, M. Ryczkowski, K. Suxho, and L. Trifyllis, SmeftFR v3 – Feynman rules generator for the Standard Model Effective Field Theory, *Comput. Phys. Commun.* **294**, 108943 (2024), arXiv:2302.01353 [hep-ph].

- [14] I. Brivio, Y. Jiang, and M. Trott, The SMEFTsim package, theory and tools, *JHEP* **12**, 070, arXiv:1709.06492 [hep-ph].
- [15] I. Brivio, SMEFTsim 3.0 — a practical guide, *JHEP* **04**, 073, arXiv:2012.11343 [hep-ph].
- [16] M. J. Baker, J. Fuentes-Martín, G. Isidori, and M. König, High- p_T signatures in vector-leptoquark models, *Eur. Phys. J. C* **79**, 334 (2019), arXiv:1901.10480 [hep-ph].
- [17] C. Zhang and S.-Y. Zhou, Convex Geometry Perspective on the (Standard Model) Effective Field Theory Space, *Phys. Rev. Lett.* **125**, 201601 (2020), arXiv:2005.03047 [hep-ph].
- [18] C. de Rham, S. Kundu, M. Reece, A. J. Tolley, and S.-Y. Zhou, Snowmass White Paper: UV Constraints on IR Physics, in *Snowmass 2021* (2022) arXiv:2203.06805 [hep-th].
- [19] A. Biekötter, L. E. G. Maskos, and B. D. Pecjak, Threshold corrections in SMEFT, (2026), arXiv:2601.15901 [hep-ph].
- [20] I. Brivio and M. Trott, The Standard Model as an Effective Field Theory, *Phys. Rept.* **793**, 1 (2019), arXiv:1706.08945 [hep-ph].
- [21] Z. Han and W. Skiba, Effective theory analysis of precision electroweak data, *Phys. Rev. D* **71**, 075009 (2005), arXiv:hep-ph/0412166.
- [22] V. Cirigliano, M. Gonzalez-Alonso, and M. L. Graesser, Non-standard Charged Current Interactions: beta decays versus the LHC, *JHEP* **02**, 046, arXiv:1210.4553 [hep-ph].
- [23] C.-Y. Chen, S. Dawson, and C. Zhang, Electroweak Effective Operators and Higgs Physics, *Phys. Rev. D* **89**, 015016 (2014), arXiv:1311.3107 [hep-ph].
- [24] J. Ellis, V. Sanz, and T. You, Complete Higgs Sector Constraints on Dimension-6 Operators, *JHEP* **07**, 036, arXiv:1404.3667 [hep-ph].
- [25] J. D. Wells and Z. Zhang, Precision Electroweak Analysis after the Higgs Boson Discovery, *Phys. Rev. D* **90**, 033006 (2014), arXiv:1406.6070 [hep-ph].
- [26] C. Hartmann, W. Shepherd, and M. Trott, The Z decay width in the SMEFT: y_t and λ corrections at one loop, *JHEP* **03**, 060, arXiv:1611.09879 [hep-ph].
- [27] V. Cirigliano, W. Dekens, J. de Vries, and E. Mereghetti, Constraining the top-Higgs sector of the Standard Model Effective Field Theory, *Phys. Rev. D* **94**, 034031 (2016), arXiv:1605.04311 [hep-ph].
- [28] A. Falkowski, M. González-Alonso, and K. Mimouni, Compilation of low-energy constraints on 4-fermion operators in the SMEFT, *JHEP* **08**, 123, arXiv:1706.03783 [hep-ph].

- [29] J. de Blas, M. Ciuchini, E. Franco, S. Mishima, M. Pierini, L. Reina, and L. Silvestrini, Electroweak precision observables and Higgs-boson signal strengths in the Standard Model and beyond: present and future, *JHEP* **12**, 135, arXiv:1608.01509 [hep-ph].
- [30] N. P. Hartland, F. Maltoni, E. R. Nocera, J. Rojo, E. Slade, E. Vryonidou, and C. Zhang, A Monte Carlo global analysis of the Standard Model Effective Field Theory: the top quark sector, *JHEP* **04**, 100, arXiv:1901.05965 [hep-ph].
- [31] A. Biekötter, T. Corbett, and T. Plehn, The Gauge-Higgs Legacy of the LHC Run II, *SciPost Phys.* **6**, 064 (2019), arXiv:1812.07587 [hep-ph].
- [32] C. Grojean, M. Montull, and M. Riembau, Diboson at the LHC vs LEP, *JHEP* **03**, 020, arXiv:1810.05149 [hep-ph].
- [33] J. Baglio, S. Dawson, S. Homiller, S. D. Lane, and I. M. Lewis, Validity of standard model EFT studies of VH and VV production at NLO, *Phys. Rev. D* **101**, 115004 (2020), arXiv:2003.07862 [hep-ph].
- [34] R. Boughezal, F. Petriello, and D. Wiegand, Removing flat directions in standard model EFT fits: How polarized electron-ion collider data can complement the LHC, *Phys. Rev. D* **101**, 116002 (2020), arXiv:2004.00748 [hep-ph].
- [35] R. Boughezal, C.-Y. Chen, F. Petriello, and D. Wiegand, Four-lepton Z boson decay constraints on the standard model EFT, *Phys. Rev. D* **103**, 055015 (2021), arXiv:2010.06685 [hep-ph].
- [36] J. J. Ethier, R. Gomez-Ambrosio, G. Magni, and J. Rojo, SMEFT analysis of vector boson scattering and diboson data from the LHC Run II, *Eur. Phys. J. C* **81**, 560 (2021), arXiv:2101.03180 [hep-ph].
- [37] S. Carrazza, C. Degrande, S. Iranipour, J. Rojo, and M. Ubiali, Can New Physics hide inside the proton?, *Phys. Rev. Lett.* **123**, 132001 (2019), arXiv:1905.05215 [hep-ph].
- [38] J. Ellis, C. W. Murphy, V. Sanz, and T. You, Updated Global SMEFT Fit to Higgs, Diboson and Electroweak Data, *JHEP* **06**, 146, arXiv:1803.03252 [hep-ph].
- [39] S. Dawson, P. P. Giardino, and A. Ismail, Standard model EFT and the Drell-Yan process at high energy, *Phys. Rev. D* **99**, 035044 (2019), arXiv:1811.12260 [hep-ph].
- [40] S. Alioli, R. Boughezal, E. Mereghetti, and F. Petriello, Novel angular dependence in Drell-Yan lepton production via dimension-8 operators, *Phys. Lett. B* **809**, 135703 (2020), arXiv:2003.11615 [hep-ph].

- [41] R. Boughezal, E. Mereghetti, and F. Petriello, Dilepton production in the SMEFT at $O(1/\Lambda^4)$, *Phys. Rev. D* **104**, 095022 (2021), [arXiv:2106.05337 \[hep-ph\]](#).
- [42] T. Cohen, X. Lu, and Z. Zhang, STrEAMlining EFT Matching, *SciPost Phys.* **10**, 098 (2021), [arXiv:2012.07851 \[hep-ph\]](#).
- [43] X. Li, K. Mimasu, K. Yamashita, C. Yang, C. Zhang, and S.-Y. Zhou, Moments for positivity: using Drell-Yan data to test positivity bounds and reverse-engineer new physics, *JHEP* **10**, 107, [arXiv:2204.13121 \[hep-ph\]](#).
- [44] S. Dawson, D. Fontes, S. Homiller, and M. Sullivan, Role of dimension-eight operators in an EFT for the 2HDM, *Phys. Rev. D* **106**, 055012 (2022), [arXiv:2205.01561 \[hep-ph\]](#).
- [45] A. Tumasyan *et al.* (CMS), Measurement of the mass dependence of the transverse momentum of lepton pairs in Drell-Yan production in proton-proton collisions at $\sqrt{s} = 13$ TeV, *Eur. Phys. J. C* **83**, 628 (2023), [arXiv:2205.04897 \[hep-ex\]](#).
- [46] R. Grober, M. Muhlleitner, M. Spira, and J. Streicher, NLO QCD Corrections to Higgs Pair Production including Dimension-6 Operators, *JHEP* **09**, 092, [arXiv:1504.06577 \[hep-ph\]](#).
- [47] C. Zhang, Single Top Production at Next-to-Leading Order in the Standard Model Effective Field Theory, *Phys. Rev. Lett.* **116**, 162002 (2016), [arXiv:1601.06163 \[hep-ph\]](#).
- [48] G. Passarino and M. Trott, The Standard Model Effective Field Theory and Next to Leading Order, (2016), [arXiv:1610.08356 \[hep-ph\]](#).
- [49] C. Englert, P. Galler, and C. D. White, Effective field theory and scalar extensions of the top quark sector, *Phys. Rev. D* **101**, 035035 (2020), [arXiv:1908.05588 \[hep-ph\]](#).
- [50] S. Dawson, M. Forslund, and P. P. Giardino, NLO SMEFT electroweak corrections to Higgs boson decays to four leptons in the narrow width approximation, *Phys. Rev. D* **111**, 015016 (2025), [arXiv:2411.08952 \[hep-ph\]](#).
- [51] L. Bellafronte, S. Dawson, C. Del Pio, M. Forslund, and P. P. Giardino, Complete NLO SMEFT Electroweak Corrections to Higgs Decays, (2025), [arXiv:2508.14966 \[hep-ph\]](#).
- [52] L. Bellafronte, S. Dawson, C. Del Pio, M. Forslund, and P. P. Giardino, Higgs Decays at NLO in the SMEFT, (2026), [arXiv:2601.09599 \[hep-ph\]](#).
- [53] J. Alwall, R. Frederix, S. Frixione, V. Hirschi, F. Maltoni, O. Mattelaer, H. S. Shao, T. Stelzer, P. Torrielli, and M. Zaro, The automated computation of tree-level and next-to-leading order differential cross sections, and their matching to parton shower simulations, *JHEP* **07**, 079, [arXiv:1405.0301 \[hep-ph\]](#).

- [54] C. Degrande, G. Durieux, F. Maltoni, K. Mimasu, E. Vryonidou, and C. Zhang, Automated one-loop computations in the standard model effective field theory, *Phys. Rev. D* **103**, 096024 (2021), arXiv:2008.11743 [hep-ph].
- [55] N. Kidonakis and A. Tonero, SMEFT chromomagnetic dipole operator contributions to $t\bar{t}$ production at approximate NNLO in QCD, *Eur. Phys. J. C* **84**, 591 (2024), arXiv:2309.16758 [hep-ph].
- [56] G. Aad *et al.* (ATLAS), Evidence for the associated production of a W boson and a top quark in ATLAS at $\sqrt{s} = 7$ TeV, *Phys. Lett. B* **716**, 142 (2012), arXiv:1205.5764 [hep-ex].
- [57] S. Chatrchyan *et al.* (CMS), Evidence for Associated Production of a Single Top Quark and W Boson in pp Collisions at $\sqrt{s} = 7$ TeV, *Phys. Rev. Lett.* **110**, 022003 (2013), arXiv:1209.3489 [hep-ex].
- [58] S. Chatrchyan *et al.* (CMS), Observation of the Associated Production of a Single Top Quark and a W Boson in pp Collisions at $\sqrt{s} = 8$ TeV, *Phys. Rev. Lett.* **112**, 231802 (2014), arXiv:1401.2942 [hep-ex].
- [59] G. Aad *et al.* (ATLAS), Measurement of the production cross-section of a single top quark in association with a W boson at 8 TeV with the ATLAS experiment, *JHEP* **01**, 064, arXiv:1510.03752 [hep-ex].
- [60] M. Aaboud *et al.* (ATLAS), Measurement of the cross-section for producing a W boson in association with a single top quark in pp collisions at $\sqrt{s} = 13$ TeV with ATLAS, *JHEP* **01**, 063, arXiv:1612.07231 [hep-ex].
- [61] M. Aaboud *et al.* (ATLAS), Measurement of differential cross-sections of a single top quark produced in association with a W boson at $\sqrt{s} = 13$ TeV with ATLAS, *Eur. Phys. J. C* **78**, 186 (2018), arXiv:1712.01602 [hep-ex].
- [62] A. M. Sirunyan *et al.* (CMS), Measurement of the production cross section for single top quarks in association with W bosons in proton-proton collisions at $\sqrt{s} = 13$ TeV, *JHEP* **10**, 117, arXiv:1805.07399 [hep-ex].
- [63] M. Aaboud *et al.* (ATLAS, CMS), Combinations of single-top-quark production cross-section measurements and $-f_{LV}V_{tb}$ —determinations at $\sqrt{s} = 7$ and 8 TeV with the ATLAS and CMS experiments, *JHEP* **05**, 088, arXiv:1902.07158 [hep-ex].
- [64] G. Aad *et al.* (ATLAS), Measurement of single top-quark production in association with a W boson in the single-lepton channel at $\sqrt{s} = 8$ TeV with the ATLAS detector, *Eur. Phys.*

J. C **81**, 720 (2021), arXiv:2007.01554 [hep-ex].

[65] A. Tumasyan *et al.* (CMS), Observation of tW production in the single-lepton channel in pp collisions at $\sqrt{s} = 13$ TeV, *JHEP* **11**, 111, arXiv:2109.01706 [hep-ex].

[66] A. Tumasyan *et al.* (CMS), Measurement of inclusive and differential cross sections for single top quark production in association with a W boson in proton-proton collisions at $\sqrt{s} = 13$ TeV, *JHEP* **07**, 046, arXiv:2208.00924 [hep-ex].

[67] G. Aad *et al.* (ATLAS), Measurement of single top-quark production in association with a W boson in pp collisions at $s=13$ TeV with the ATLAS detector, *Phys. Rev. D* **110**, 072010 (2024), arXiv:2407.15594 [hep-ex].

[68] A. Hayrapetyan *et al.* (CMS), Measurement of inclusive and differential cross sections of single top quark production in association with a W boson in proton-proton collisions at $\sqrt{s} = 13.6$ TeV, *JHEP* **01**, 107, arXiv:2409.06444 [hep-ex].

[69] G. A. Ladinsky and C. P. Yuan, The W - top background to heavy Higgs production, *Phys. Rev. D* **43**, 789 (1991).

[70] A. Heinson, A. S. Belyaev, and E. E. Boos, Single top quarks at the Fermilab Tevatron, *Phys. Rev. D* **56**, 3114 (1997), arXiv:hep-ph/9612424.

[71] S. Moretti, Single top production in the t W+ channel and Higgs signals via $H \rightarrow W^+ W^-$ at the Large Hadron Collider, *Phys. Rev. D* **56**, 7427 (1997), arXiv:hep-ph/9705388.

[72] A. S. Belyaev, E. E. Boos, and L. V. Dudko, Single top quark at future hadron colliders: Complete signal and background study, *Phys. Rev. D* **59**, 075001 (1999), arXiv:hep-ph/9806332.

[73] T. M. P. Tait, The tW^- mode of single top production, *Phys. Rev. D* **61**, 034001 (1999), arXiv:hep-ph/9909352.

[74] A. Belyaev and E. Boos, Single top quark tW + X production at the CERN LHC: A Closer look, *Phys. Rev. D* **63**, 034012 (2001), arXiv:hep-ph/0003260.

[75] S. Zhu, Next-to-leading order QCD corrections to $bg \rightarrow tW^-$ at CERN large hadron collider, *Phys. Lett. B* **524**, 283 (2002), [Erratum: *Phys.Lett.B* 537, 351–352 (2002)], arXiv:hep-ph/0109269.

[76] J. M. Campbell and F. Tramontano, Next-to-leading order corrections to Wt production and decay, *Nucl. Phys. B* **726**, 109 (2005), arXiv:hep-ph/0506289.

[77] Q.-H. Cao, Demonstration of One Cutoff Phase Space Slicing Method: Next-to-Leading Order QCD Corrections to the tW Associated Production in Hadron Collision, (2008),

arXiv:0801.1539 [hep-ph].

[78] S. Frixione, E. Laenen, P. Motylinski, B. R. Webber, and C. D. White, Single-top hadroproduction in association with a W boson, *JHEP* **07**, 029, arXiv:0805.3067 [hep-ph].

[79] E. Re, Single-top Wt -channel production matched with parton showers using the POWHEG method, *Eur. Phys. J. C* **71**, 1547 (2011), arXiv:1009.2450 [hep-ph].

[80] L.-B. Chen and J. Wang, Analytic two-loop master integrals for tW production at hadron colliders: I *, *Chin. Phys. C* **45**, 123106 (2021), arXiv:2106.12093 [hep-ph].

[81] M.-M. Long, R.-Y. Zhang, W.-G. Ma, Y. Jiang, L. Han, Z. Li, and S.-S. Wang, Two-loop master integrals for the single top production associated with W boson, (2021), arXiv:2111.14172 [hep-ph].

[82] L.-B. Chen, L. Dong, H. T. Li, Z. Li, J. Wang, and Y. Wang, One-loop squared amplitudes for hadronic tW production at next-to-next-to-leading order in QCD, *JHEP* **08**, 211, arXiv:2204.13500 [hep-ph].

[83] J. Wang and Y. Wang, Analytic two-loop master integrals for tW production at hadron colliders. Part II, *JHEP* **02**, 127, arXiv:2211.13713 [hep-ph].

[84] L.-B. Chen, L. Dong, H. T. Li, Z. Li, J. Wang, and Y. Wang, Analytic two-loop QCD amplitudes for tW production: Leading color and light fermion-loop contributions, *Phys. Rev. D* **106**, 096029 (2022), arXiv:2208.08786 [hep-ph].

[85] L.-B. Chen, L. Dong, H. T. Li, Z. Li, J. Wang, and Y. Wang, Complete two-loop QCD amplitudes for tW production at hadron colliders, *JHEP* **07**, 089, arXiv:2212.07190 [hep-ph].

[86] N. Kidonakis, Single top production at the Tevatron: Threshold resummation and finite-order soft gluon corrections, *Phys. Rev. D* **74**, 114012 (2006), arXiv:hep-ph/0609287.

[87] N. Kidonakis, Higher-order soft gluon corrections in single top quark production at the LHC, *Phys. Rev. D* **75**, 071501 (2007), arXiv:hep-ph/0701080.

[88] N. Kidonakis, Two-loop soft anomalous dimensions for single top quark associated production with a W^- or H^- , *Phys. Rev. D* **82**, 054018 (2010), arXiv:1005.4451 [hep-ph].

[89] N. Kidonakis, NNLL threshold resummation for top-pair and single-top production, *Phys. Part. Nucl.* **45**, 714 (2014), arXiv:1210.7813 [hep-ph].

[90] N. Kidonakis, Top Quark Production, in *Helmholtz International Summer School on Physics of Heavy Quarks and Hadrons* (2014) pp. 139–168, arXiv:1311.0283 [hep-ph].

- [91] N. Kidonakis, Single-top transverse-momentum distributions at approximate NNLO, *Phys. Rev. D* **93**, 054022 (2016), arXiv:1510.06361 [hep-ph].
- [92] N. Kidonakis, Soft-gluon corrections for tW production at N^3LO , *Phys. Rev. D* **96**, 034014 (2017), arXiv:1612.06426 [hep-ph].
- [93] N. Kidonakis, Soft-gluon corrections in top-quark production, *Int. J. Mod. Phys. A* **33**, 1830021 (2018), arXiv:1806.03336 [hep-ph].
- [94] N. Kidonakis, Soft anomalous dimensions for single-top production at three loops, *Phys. Rev. D* **99**, 074024 (2019), arXiv:1901.09928 [hep-ph].
- [95] N. Kidonakis and N. Yamanaka, Higher-order corrections for tW production at high-energy hadron colliders, *JHEP* **05**, 278, arXiv:2102.11300 [hep-ph].
- [96] N. Kidonakis, NNLL resummation for s-channel single top quark production, *Phys. Rev. D* **81**, 054028 (2010), arXiv:1001.5034 [hep-ph].
- [97] N. Kidonakis, Next-to-next-to-leading-order collinear and soft gluon corrections for t-channel single top quark production, *Phys. Rev. D* **83**, 091503 (2011), arXiv:1103.2792 [hep-ph].
- [98] N. Kidonakis, Top-quark transverse-momentum distributions in t-channel single-top production, *Phys. Rev. D* **88**, 031504 (2013), arXiv:1306.3592 [hep-ph].
- [99] N. Kidonakis, Resummation for s -channel single-top production, (2025), arXiv:2502.17631 [hep-ph].
- [100] C. S. Li, H. T. Li, D. Y. Shao, and J. Wang, Momentum-space threshold resummation in tW production at the LHC, *JHEP* **06**, 125, arXiv:1903.01646 [hep-ph].
- [101] J.-L. Ding, H. T. Li, and J. Wang, Next-to-next-to-leading order threshold soft function for tW production, *JHEP* **05**, 143, arXiv:2502.18648 [hep-ph].
- [102] J.-L. Ding, H. T. Li, and J. Wang, Approximate N^2LO and N^3LO QCD Predictions for tW Production, (2025), arXiv:2512.10711 [hep-ph].
- [103] T. Hahn, Generating Feynman diagrams and amplitudes with FeynArts 3, *Comput. Phys. Commun.* **140**, 418 (2001), arXiv:hep-ph/0012260.
- [104] V. Shtabovenko, R. Mertig, and F. Orellana, New Developments in FeynCalc 9.0, *Comput. Phys. Commun.* **207**, 432 (2016), arXiv:1601.01167 [hep-ph].
- [105] V. Shtabovenko, R. Mertig, and F. Orellana, FeynCalc 9.3: New features and improvements, *Comput. Phys. Commun.* **256**, 107478 (2020), arXiv:2001.04407 [hep-ph].

- [106] V. Shtabovenko, R. Mertig, and F. Orellana, FeynCalc 10: Do multiloop integrals dream of computer codes?, (2023), [arXiv:2312.14089 \[hep-ph\]](https://arxiv.org/abs/2312.14089).
- [107] R. Mertig, M. Bohm, and A. Denner, FEYN CALC: Computer algebraic calculation of Feynman amplitudes, *Comput. Phys. Commun.* **64**, 345 (1991).
- [108] A. Buckley, J. Ferrando, S. Lloyd, K. Nordström, B. Page, M. Rüfenacht, M. Schönherr, and G. Watt, LHAPDF6: parton density access in the LHC precision era, *Eur. Phys. J. C* **75**, 132 (2015), [arXiv:1412.7420 \[hep-ph\]](https://arxiv.org/abs/1412.7420).
- [109] G. P. Lepage, Adaptive multidimensional integration: VEGAS enhanced, *J. Comput. Phys.* **439**, 110386 (2021), [arXiv:2009.05112 \[physics.comp-ph\]](https://arxiv.org/abs/2009.05112).
- [110] G. P. Lepage, gplepage/vegas: vegas version 6.1.2, Zenodo, May 21, 2024. DOI: [10.5281/zenodo.11238512](https://doi.org/10.5281/zenodo.11238512).
- [111] P. Mastrolia, E. Mirabella, and T. Peraro, Integrand reduction of one-loop scattering amplitudes through Laurent series expansion, *JHEP* **06**, 095, [Erratum: *JHEP* 11, 128 (2012)], [arXiv:1203.0291 \[hep-ph\]](https://arxiv.org/abs/1203.0291).
- [112] T. Peraro, Ninja: Automated Integrand Reduction via Laurent Expansion for One-Loop Amplitudes, *Comput. Phys. Commun.* **185**, 2771 (2014), [arXiv:1403.1229 \[hep-ph\]](https://arxiv.org/abs/1403.1229).
- [113] V. Hirschi and T. Peraro, Tensor integrand reduction via Laurent expansion, *JHEP* **06**, 060, [arXiv:1604.01363 \[hep-ph\]](https://arxiv.org/abs/1604.01363).
- [114] A. Denner, S. Dittmaier, and L. Hofer, Collier: a fortran-based Complex One-Loop Library in Extended Regularizations, *Comput. Phys. Commun.* **212**, 220 (2017), [arXiv:1604.06792 \[hep-ph\]](https://arxiv.org/abs/1604.06792).
- [115] S. Bailey, T. Cridge, L. A. Harland-Lang, A. D. Martin, and R. S. Thorne, Parton distributions from LHC, HERA, Tevatron and fixed target data: MSHT20 PDFs, *Eur. Phys. J. C* **81**, 341 (2021), [arXiv:2012.04684 \[hep-ph\]](https://arxiv.org/abs/2012.04684).
- [116] F. Cornet-Gomez, V. Miralles, M. Miralles López, M. Moreno Llácer, and M. Vos, Future collider constraints on top-quark operators, *JHEP* **10**, 156, [arXiv:2503.11518 \[hep-ph\]](https://arxiv.org/abs/2503.11518).
- [117] E. Celada, T. Giani, J. ter Hoeve, L. Mantani, J. Rojo, A. N. Rossia, M. O. A. Thomas, and E. Vryonidou, Mapping the SMEFT at high-energy colliders: from LEP and the (HL-)LHC to the FCC-ee, *JHEP* **09**, 091, [arXiv:2404.12809 \[hep-ph\]](https://arxiv.org/abs/2404.12809).
- [118] G. Aad *et al.* (ATLAS), Inclusive and differential cross-sections for dilepton $t\bar{t}$ production measured in $\sqrt{s} = 13$ TeV pp collisions with the ATLAS detector, *JHEP* **07**, 141,

arXiv:2303.15340 [hep-ex].

[119] A. Tumasyan *et al.* (CMS), Measurement of differential $t\bar{t}$ production cross sections in the full kinematic range using lepton+jets events from proton-proton collisions at $\sqrt{s} = 13$ TeV, *Phys. Rev. D* **104**, 092013 (2021), arXiv:2108.02803 [hep-ex].